REFERENCE: **SAF/O3M/KNMI/VR/001**
ISSUE: 4/2013
DATE: 25 June 2013
PAGES: 50

O3M SAF VALIDATION REPORT

Validated products:

Identifier	Name	Acronym
O3M-14	Offline Absorbing Aerosol Index from MetOp-A	ARS/AAI
O3M-70	Offline Absorbing Aerosol Index from MetOp-B	ARS/AAI
O3M-61	NRT Absorbing Aerosol Index from MetOp-A	NAR/AAI
O3M-71	NRT Absorbing Aerosol Index from MetOp-B	NAR/AAI
O3M-63	Offline Absorbing Aerosol Index from MetOp-A PMDs	ARP/AAI
O3M-73	Offline Absorbing Aerosol Index from MetOp-B PMDs	ARP/AAI
O3M-62	NRT Absorbing Aerosol Index from MetOp-A PMDs	NAP/AAI
O3M-72	NRT Absorbing Aerosol Index from MetOp-B PMDs	NAP/AAI

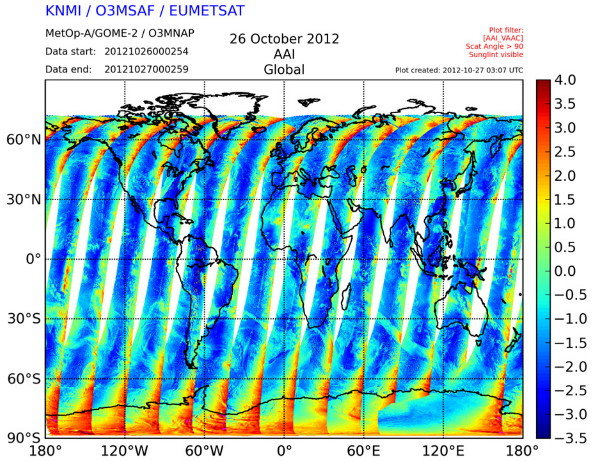

Authors:

Name	Institute
L.G. Tilstra	Royal Netherlands Meteorological Institute (KNMI)
O.N.E. Tuinder	Royal Netherlands Meteorological Institute (KNMI)
P. Stammes	Royal Netherlands Meteorological Institute (KNMI)

Reporting period: January 2007 – May 2013

Input data versions: GOME-2 level 1b version 4.0, 4.1, 4.2, 4.3, 4.4, 4.5, 5.0, 5.1, 5.2, 5.3

Data processor versions: OPERA version 1.18, 1.20, 1.21, 1.22, 1.23, 1.25, 1.26, 1.28

Abstract

This document presents verification results for the Absorbing Aerosol Index (AAI) produced by KNMI within the framework of the EUMETSAT Satellite Application Facility on Ozone and Atmospheric Chemistry Monitoring (O3M SAF). The AAI is capable of detecting aerosols over land and sea surfaces, and even in the presence of clouds when the absorbing aerosol layer overlies the clouds. As a result, it is a commonly used tool for aerosol screening. For O3M SAF data users the AAI from GOME-2 on the Metop-A satellite is available from January 2007 on, and from December 2012 onwards also AAI data from GOME-2 on the Metop-B platform will become available.

In this report, the GOME-2 AAI product is compared with the OMI-TOMS AAI product from NASA for a collection of days with clear aerosol events. The comparison shows that the maximum AAI values from the GOME-2 product are in the same locations as the AAI maxima from the OMI-TOMS product, but that the GOME-2 AAI value is somewhat lower than the OMI-TOMS AAI value. A direct intercomparison between the SCIAMACHY and GOME-2 AAI shows a good correlation between the two data sets, and points to a near-zero offset in the GOME-2 AAI. Statistical analyses of the GOME-2 AAI confirm this, and show physically sound behaviour. An East-West bias is present in the GOME-2 AAI in the Southern Hemisphere, south of the so-called 'C-shape' polarisation correction phenomenon.

Note that the verification presented in this report was applied to data to which a correction for instrument degradation was not applied.

Contents

Chapter 1

Introduction

1.1 General

This document presents the results of a verification study of the Absorbing Aerosol Index (AAI) level-2 product produced by the Royal Netherlands Meteorological Institute (KNMI) within the framework of the EUMETSAT Satellite Application Facility on Ozone and Atmospheric Chemistry Monitoring (O3M SAF). The AAI indicates the presence of UV-absorbing aerosols, like desert dust from dust storms and smoke from biomass burning events (see, for instance, *de Graaf et al.* [2010]). The AAI produced by the O3M SAF is calculated from the reflectances at 340 and 380 nm measured by the GOME-2 instruments on Metop-A/B operated by EUMETSAT. The verification consists of a comparison of daily GOME-2 AAI maps with similar maps from the OMI-TOMS AAI, a direct intercomparison of the AAI from SCIAMACHY and GOME-2, and verification of the statistical properties of the GOME-2 data.

1.2 O3M SAF

The EUMETSAT Satellite Application Facility on Ozone and Atmospheric Chemistry Monitoring (O3M SAF) has been developed to provide good quality data for monitoring and research of atmospheric chemistry. More specifically, the O3M SAF processes, archives, validates and disseminates atmospheric data products of ozone, various trace gases such as SO_2 and NO_2, aerosols and surface ultraviolet radiation using the measurements performed by the Meteorological Operational (MetOp) satellites of EUMETSAT.

More information on the O3M SAF and available data can be found on the following web page:

http://o3msaf.fmi.fi/

1.3 AAI from GOME-2

The AAI is an operational product in the O3M SAF and is produced in the same operational chain as the operational NOP/OOP product. The GOME-2 level-1b data used for this verification study were generated by PPF 4.0 and above. More specifically, reprocessed GOME-2 level-1b data were used from 5 January 2007 to 26 June 2008 (the so-called 'R01 reprocessing'), and after this date the data were taken from the regular NRT flow of level-1b PDU data products that were disseminated by EUMETSAT via EUMETCast. The Metop-A/B level-1b (PPF) and Product Generation Element (PGE) versions of the AAI data discussed in this verification report can be found in Tables 1.1 and 1.2 of section 1.5.

The GOME-2 AAI products are calculated for both the Metop-A and Metop-B satellite instruments. Next to the original AAI product that is derived from the main science channels (MSC), also AAI products derived from the polarisation measurement device (PMD) bands are produced. These PMD AAI products have a higher spatial resolution than the original MSC AAI products, which is especially important for the study of aerosol events such as forest fires and volcanic eruptions.

In this report, GOME-2 AAI values are plotted as daily maps where the values are within the -2.5 to $+4.5$ range. This captures the most common AAI values and shows most spatial structure when plotted. AAI values larger than 4.5 are shown as the maximum value of the scale to avoid white/blank pixels. Some blocks or periods are missing, due to lack of level-1b data, or other small failures.

The name AAI is traditionally used for indicating absorbing aerosols, for which the residue has positive values. An AAI of zero would be retrieved if there is no absorbing aerosol, just Rayleigh scattering and reflection by the surface. Scattering aerosols, such as clouds, are often present in a large number of pixels and lead to a negative AAI value. We therefore also show the negative values from the AAI retrieval. More information on the behaviour of absorbing and scattering aerosols can be found in the GOME-2 Algorithm Theoretical Basis Document (ATBD) [*de Graaf et al.*, 2010].

1.4 AAI from OMI

The data set used for comparison is the OMI-TOMS AAI dataset, downloaded from the FTP address `ftp://toms.gsfc.nasa.gov/pub/omi/data/aerosol/Y2008`. The wavelength pair used for OMI is the same pair as for EP/TOMS, 331/360 nm (see `http://toms.gsfc.nasa.gov/aerosols/aerosols_v8.html`). The data are plotted as daily maps on the same grid and with the same colour scale as the GOME-2 AAI, but since the OMI-TOMS AAI product only contains values larger than 1, a large part of the image will be empty. Where AAI values larger than 4.5 were found, the value 4.5 is shown.

1.5 Processor and dataset versions

Over the course of the years, the operational Product Processor Facility (PPF) version numbers and the operational Product Generation Element (PGE) version numbers have changed. The GOME-2/Metop-A AAI data presented and verified in this report were processed from GOME-2 level-1b data produced with PPF version 4.0 and above. The PGE version used was v1.18 and v1.20 for the reprocessed data (until 20 January 2010), and v1.20–v1.28 for data after 20 January 2010, which are from the normal operational forward processing. For GOME-2/Metop-B the level-1b data were produced with PPF version 5.3 and the PGE versions used were v1.26 and v1.28. Tables 1.1 and 1.2 provide an overview of the version numbers of the GOME-2/Metop-A/B AAI datasets that were studied in this verification report.

1.6 Getting access to data

Interested users can get access to the data via the EUMETSAT UMARF, the unified meteorological archive facility. The procedure involves a registration and after this step the user can select and request the data. For more information please consult the 'Access to Data' section on the EUMETSAT website, or go directly to the UMARF archive via the following URL:

`http://archive.eumetsat.int/umarf/`

Metop-A Time Period	PPF Version	PGE Version	Processing Type
2007–01–04 — 2009–01–06	4.0	1.18	reprocessed
2009–01–07 — 2009–04–06	4.1	1.18	reprocessed
2009–04–07 — 2009–08–17	4.2	1.18	reprocessed
2009–08–18 — 2009–08–31	4.3	1.18	reprocessed
2009–09–01 — 2010–01–20	4.3	1.20	reprocessed
2010–01–21 — 2010–01–25	4.4	1.20	NRT
2010–01–26 — 2010–02–27	4.4	1.21	NRT
2010–02–28 — 2010–04–26	4.4	1.22	NRT
2010–04–27 — 2010–09–08	4.4	1.23	NRT
2010–09–09 — 2011–01–04	4.5	1.23	NRT
2011–01–05 — 2011–03–01	5.0	1.23	NRT
2011–03–02 — 2011–09–05	5.1	1.23	NRT
2011–09–06 — 2012–01–23	5.2	1.23	NRT
2012–01–24 — 2012–01–27	5.3	1.23	NRT
2012–01–28 — 2012–08–06	5.3	1.25	NRT
2012–08–07 — 2013–05–12	5.3	1.26	NRT
2013–05–13 — 2013–05–31	5.3	1.28	NRT

Table 1.1: GOME-2/Metop-A AAI: Overview of version numbers of the Product Processor Facility (PPF) and Product Generation Element (PGE) and time windows in which these were active. The last column states whether the data were reprocessed or part of the normal near-real time (NRT) forward processing.

Metop-B Time Period	PPF Version	PGE Version	Processing Type
2012–12–13 — 2013–05–12	5.3	1.26	NRT [Verification]
2012–05–13 — 2013–05–31	5.3	1.28	NRT [Verification]

Table 1.2: GOME-2/Metop-B AAI: Overview of version numbers of the Product Processor Facility (PPF) and Product Generation Element (PGE) and time windows in which these were active.

Chapter 2

Aerosol events

To show the potential of the Aerosol Absorbing Index, we have selected cases in which volcanic ash, desert dust and biomass burning events are shown.

In the first case, we show the eruption of the volcano Kasatochi in Alaska, USA, on 8 August 2008. In the second case, desert dust from the coast of west Africa is transported over the Atlantic Ocean. In the third case, aerosol from a large biomass burning event, forest fires in Siberia, is transported eastward in the direction of Alaska.

Volcanic Eruption

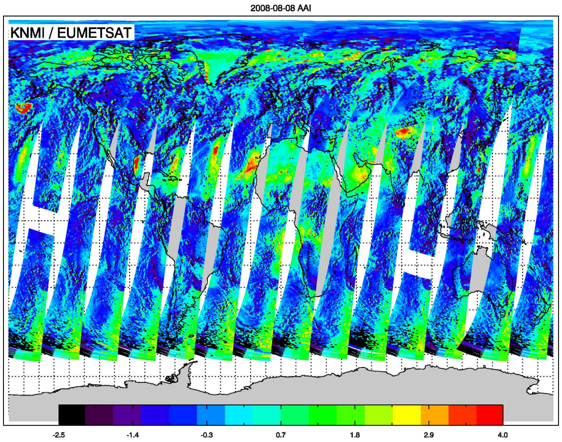

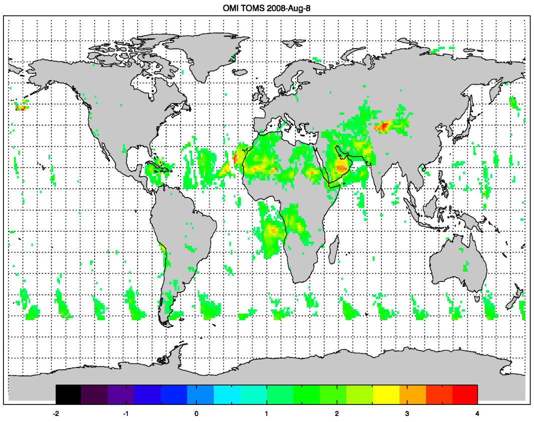

Desert Dust

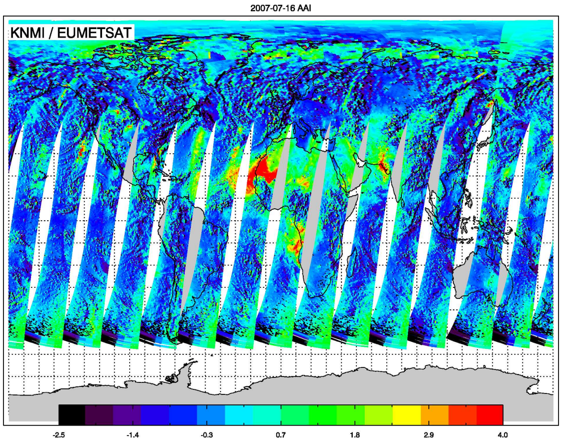
2007-07-16 AAI
KNMI / EUMETSAT
-2.5
-1.4
-0.3
0.7
1.8
2.9
4.0

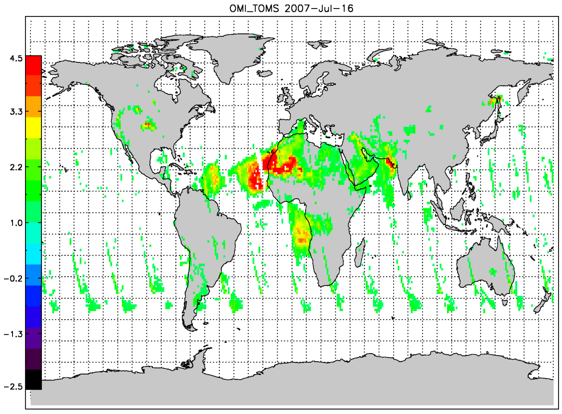
OMI_TOMS 2007-Jul-16
4.5
3.3
2.2
1.0
-0.2
-1.3
-2.5

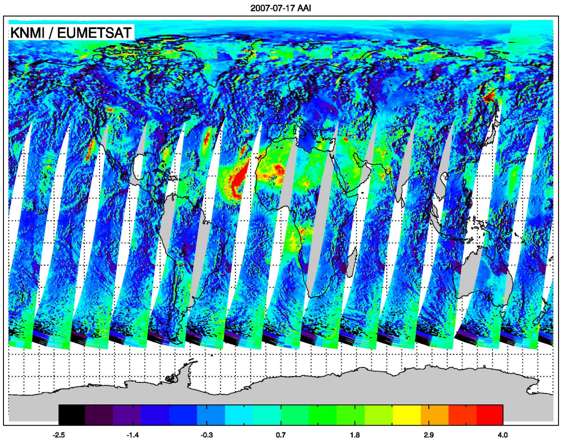
2007-07-17 AAI
KNMI / EUMETSAT
-2.5
-1.4
-0.3
0.7
1.8
2.9
4.0

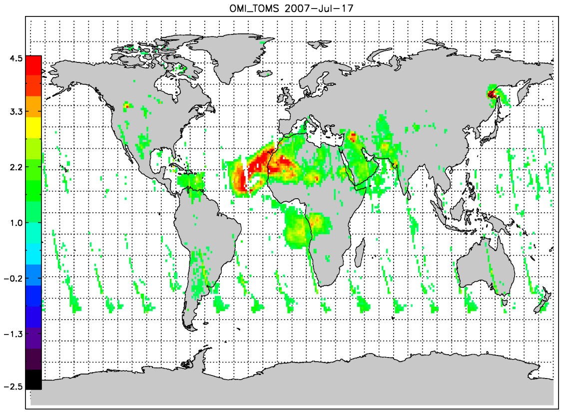
OMI_TOMS 2007-Jul-17
4.5
3.3
2.2
1.0
-0.2
-1.3
-2.5

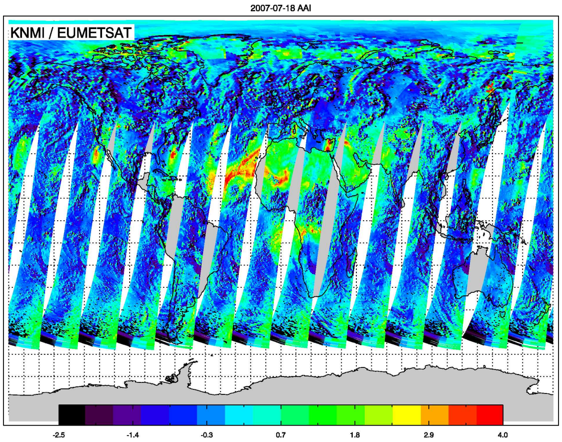
2007-07-18 AAI
KNMI / EUMETSAT
-2.5
-1.4
-0.3
0.7
1.8
2.9
4.0

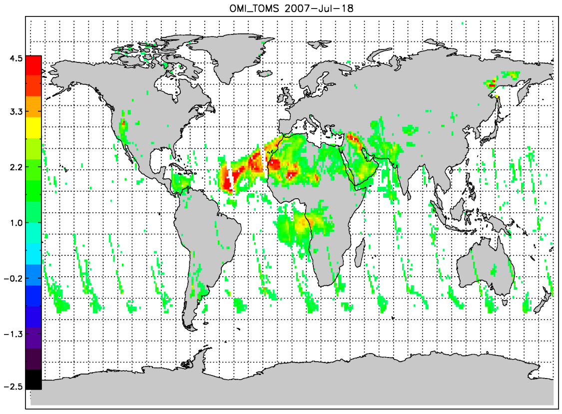
OMI_TOMS 2007-Jul-18
4.5
3.3
2.2
1.0
-0.2
-1.3
-2.5

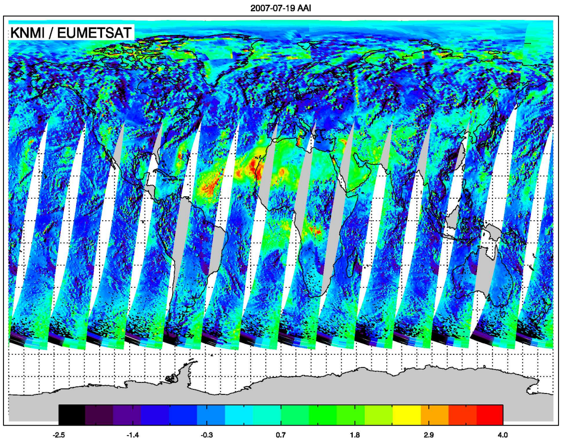
2007-07-19 AAI
KNMI / EUMETSAT
-2.5
-1.4
-0.3
0.7
1.8
2.9
4.0

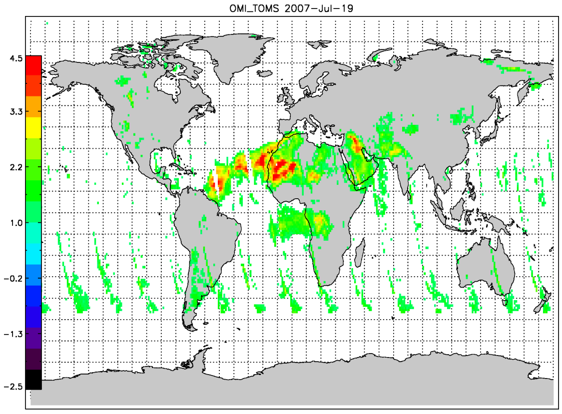
OMI_TOMS 2007-Jul-19
4.5
3.3
2.2
1.0
-0.2
-1.3
-2.5

Biomass Burning

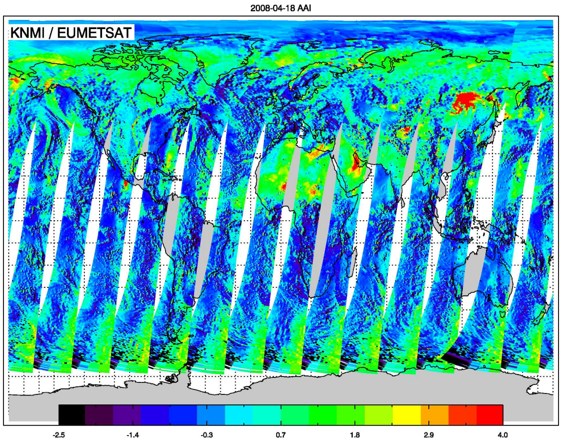

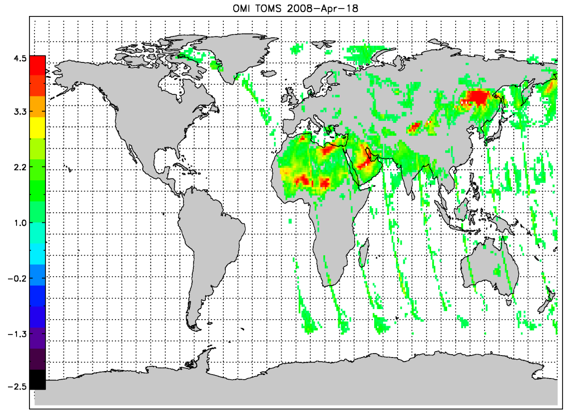

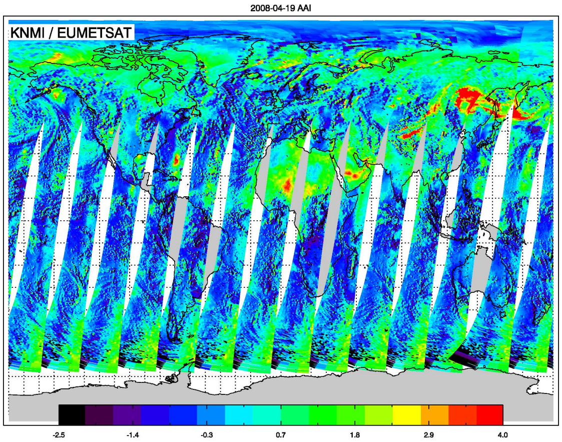

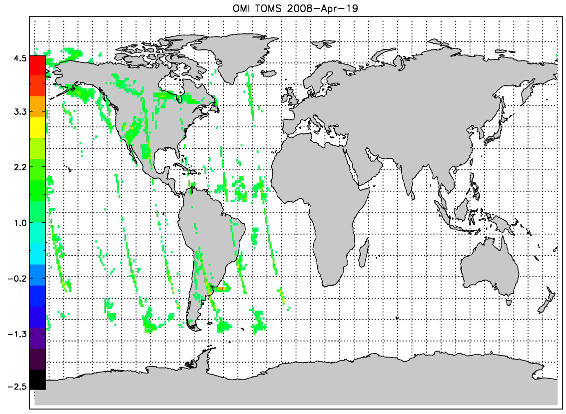

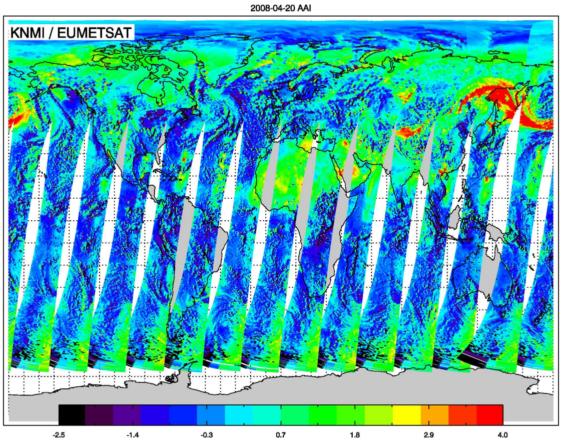

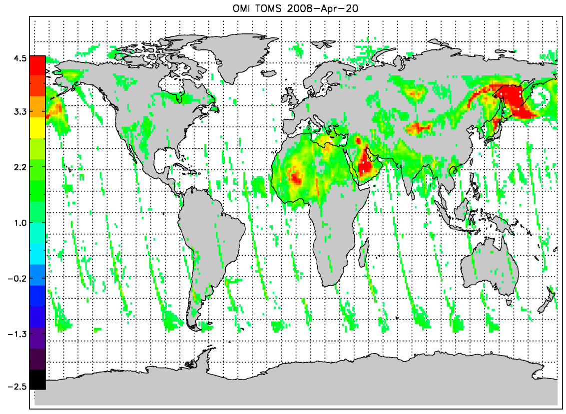

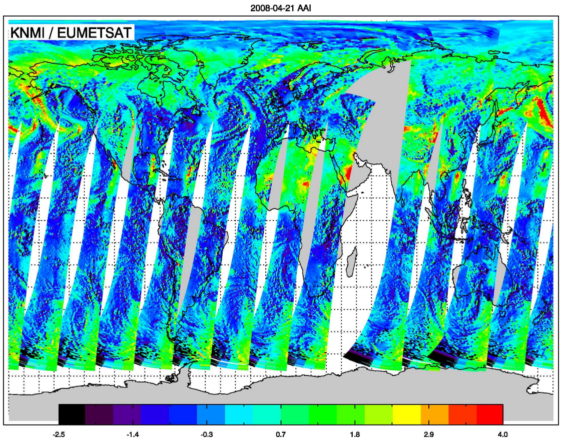

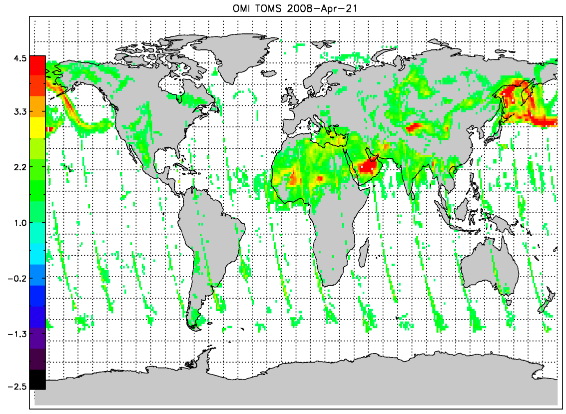

Chapter 3

SCIAMACHY versus GOME-2

3.1 Short introduction

In this chapter we perform a direct comparison between (i) the AAI measured by GOME-2, and (ii) the AAI measured by SCIAMACHY (at roughly the same time and place). Because of the slightly different orbital periods, such an intercomparison is not possible for all days of the year. However, this is not a problem, as will be explained further on. For the many days on which intercomparison is possible, the orbit tracks overlap completely, ensuring that the scattering geometries (i.e., viewing and solar angles) are nearly identical, which adds to credibility and reliability of the intercomparison.

3.2 Description of SCIAMACHY

SCIAMACHY (Scanning Imaging Absorption Spectrometer for Atmospheric Chartography) [*Bovensmann et al.*, 1999] was launched on 1 March 2002 onboard the Envisat satellite. Like GOME-2, it was launched into a near-polar, sun-synchronous orbit, with an almost identical orbital period of about 100 min. The local crossing time of the equator is 10:00 a.m., so SCIAMACHY observes a certain ground scene 30 minutes after GOME-2 does. A major difference with respect to GOME-2 is that SCIAMACHY has the ability to perform not only nadir measurements, but also limb measurements. These two measurement modes are being alternated along the orbit. The resulting data are stored in blocks, called "states". A nadir state covers an area of 960×490 km^2 (across track × along track).

The wavelength region covered by SCIAMACHY is 240–2380 nm, with a spectral resolution of 0.2–1.5 nm. The scanning sequence is similar to that of GOME-2: 4 s forward scan and a fast reverse scan in 1 s. The swath is 960 km wide, half of that of GOME-2. Another major difference with GOME-2 is that the nadir spectrum is divided into 56 wavelength regions, called "clusters", that are all read out with their own integration time (IT). This allows a higher spatial resolution for the most important spectral regions, at the expense of other wavelength regions where the spectrum is of less scientific interest, or would otherwise yield a weak signal. Typical ITs are 0.25 s (pixel size 60×30 km^2) and 0.5 s (pixel size 120×30 km^2), but 0.125 s, 1.0 s, 5 s and 10 s are also used. Owing to the alternation of nadir and limb modes, global coverage is achieved in only 6 days instead of the 1.5 days for the GOME-2 instrument.

3.3 Intercomparison approach

Figure 3.1 explains the approach that was followed in a graphical way. For a given day, in this case 17 October 2007, we gather all SCIAMACHY and GOME-2 AAI orbits that are available to us. For each SCIAMACHY orbit, we determine, in an intelligent way, the equator passing point (EPP). Using this

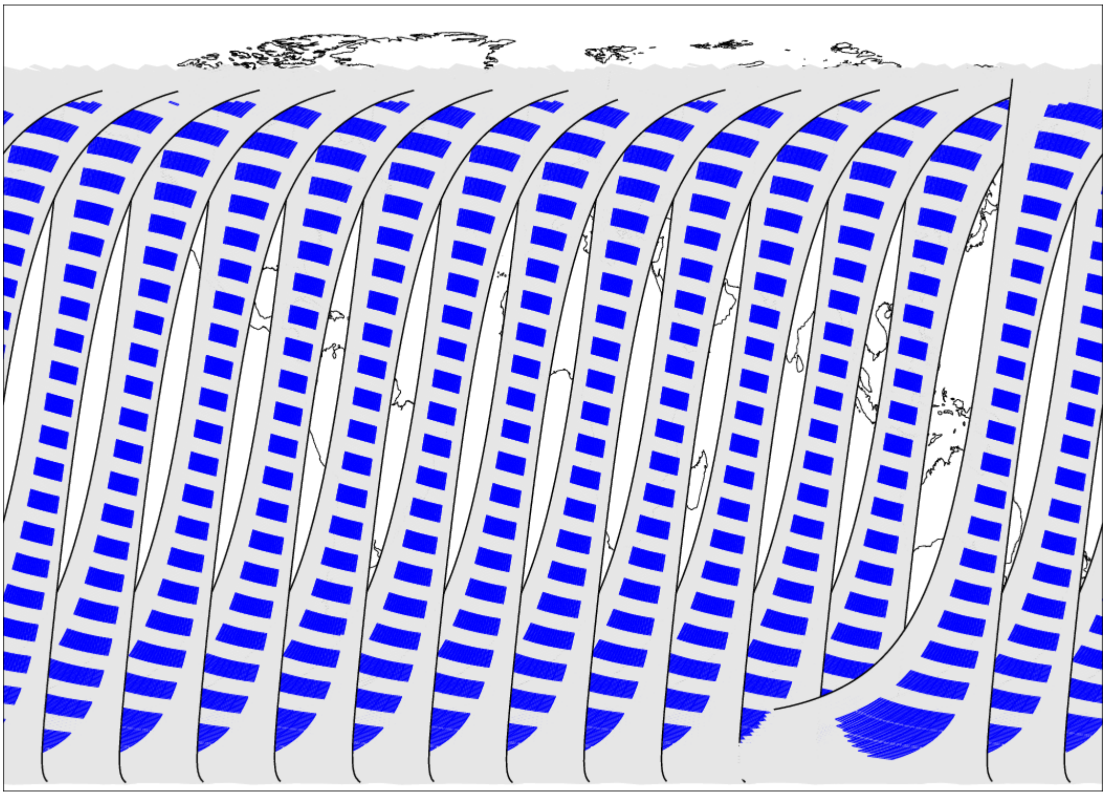

Figure 3.1: Graphical explanation of the approach that was followed to compare the GOME-2 AAI's with those determined by SCIAMACHY. The black curves indicate the borders of the GOME-2 swaths. The blue boxes indicate the individual SCIAMACHY footprints. The data are from 17 October 2007.

information, we look for the GOME-2 orbit that has a more or less identical EPP. If this orbit exists, then we have a match. Note that, because of the different equator passing times (GOME-2: 09:30 LT; SCIAMACHY: 10:00 LT), there is a 30-minutes time difference. Related to this, there is also a slight difference in the solar zenith angle (SZA) which goes up to 7 degrees near the equator.

After that, we concentrate on all SCIAMACHY forward scan pixels between 70°N and 70°S that have a SZA below 80°. For all the pixels in this subset, we start looking for the GOME-2 forward scan pixels that belong to it, record their residues, and take the mean if more than one are found. The result we will call the "collocated GOME-2 AAI" from now on. We can then analyse the results, as shown in Fig. 3.2. Here we plotted the collocated GOME-2 AAI versus the original SCIAMACHY AAI (version: SC-AAI 5.0, released 11 October 2011). The agreement is rather good, although there is quite some scatter around the expected one-to-one relationship. This scatter can be explained by a number of reasons.

First of all, we have a 30-minutes time difference between SCIAMACHY and GOME-2, which could lead to a change in the observed scene in the case of clouds. By filtering out cloudy scenes we could indeed reduce the scatter a bit, of course at the expense of the number of available data points. Secondly, there is a difference in the solar zenith and azimuth angles of SCIAMACHY and GOME-2. Thirdly, and most importantly, the SCIAMACHY and GOME-2 footprints do not overlap completely, so there will always be a spatial collocation mismatch between the SCIAMACHY and GOME-2 footprints. We took no action to improve on this, because the goal here is to analyse the entire collection of data as a whole, not to improve the intercomparison of individual ground pixels.

In Fig. 3.2 we also present a red line, which is a linear fit to the data points. Weighted fitting was not applied, but residues with values lower than -10 and higher than $+10$ were not trusted and were therefore not allowed to take part in the fitting process. For the specific day shown in Fig. 3.2, 13 July 2008, the slope was found to be 1.07 ± 0.06 and the intercept was -0.01 ± 0.05, pointing to a good agreement

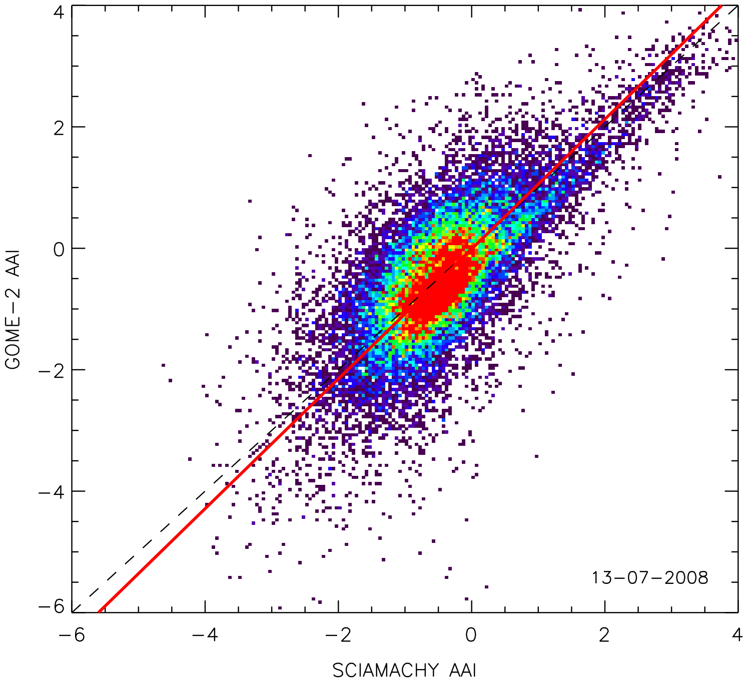

Figure 3.2: The "collocated GOME-2 AAI" versus the SCIAMACHY AAI, for 13 July 2008. The agreement is fair, considering the fact that we took no effort to improve handling the spatial mismatch between the SCIAMACHY and GOME-2 footprints. The red line is a linear fit to the data points.

between the GOME-2 AAI w.r.t. the SCIAMACHY AAI. Note that the SCIAMACHY AAI was found to be well calibrated w.r.t. GOME-2's predecessor GOME-1 [*Tilstra et al.*, 2007, 2011a].

3.4 First results – time series A

The analysis described in the previous section was performed on the entire GOME-2 AAI reprocessed data set that was available. This data set covers most of the years 2007 and 2008. While processing the data set, we recorded the number of orbits for which we could successfully link the SCIAMACHY data to GOME-2 data. When a SCIAMACHY monitoring orbit was encountered (narrow swath, nadir static, et cetera), then this orbit was skipped altogether. When a GOME-2 narrow swath or nadir static orbit was encountered, this orbit was not skipped, but it was recorded that a narrow swath/nadir static orbit was used that day. We decided to remove days with more than two of such orbits from the analysis.

Because of the slightly different orbital periods of SCIAMACHY and GOME-2, in general the orbit tracks of the two instruments do not overlap. Every nine days, however, the situation occurs that they do overlap, for a relatively short period of ∼2 days (depending on how strict we are). For each day for which we could find SCIAMACHY and GOME-2 orbits with overlapping orbit tracks, we recorded the number of these orbits. Slope and intercept of the linear fit to the collocated AAI's, performed in the way described before, were also recorded. In Fig. 3.3, we plotted the resulting slopes as a function of time. The red circles are results which in our opinion are not reliable, either because there were not enough orbit track overlaps found (say, less than 10), or because there were two or more narrow swath/nadir static orbits involved. The blue circles are the remaining results, which we expect to be reliable.

As can be seen, the red circles are scattered, but the blue circles are rather consistent in their behaviour. At first sight, there appears to be a good correlation between the SCIAMACHY and GOME-2 residues, with a slope very close to one. On the other hand, there seems to be a periodic or seasonal variation hidden behind the scatter in the slopes. In Fig. 3.4, we plotted the intercepts of the linear fits. The offset

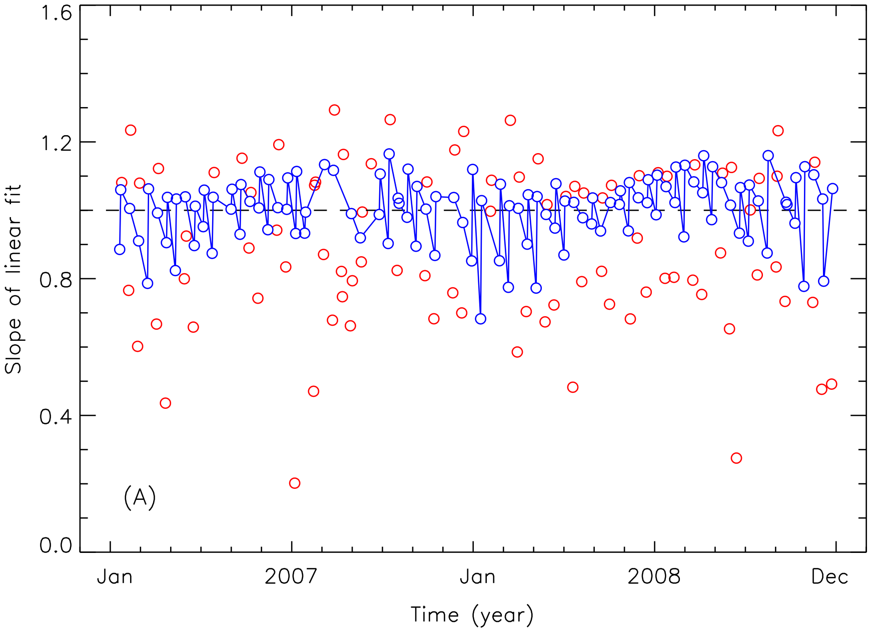

Figure 3.3: Slope of the linear fits to the (GOME-2 versus SCIAMACHY) data points as a function of time. The red circles are unreliable: not enough orbits with perfect orbit track overlap between SCIAMACHY and GOME-2, and/or too many GOME-2 narrow swath orbits included. The blue circles are believed to be reliable, although some scatter is obviously present in the blue data points.

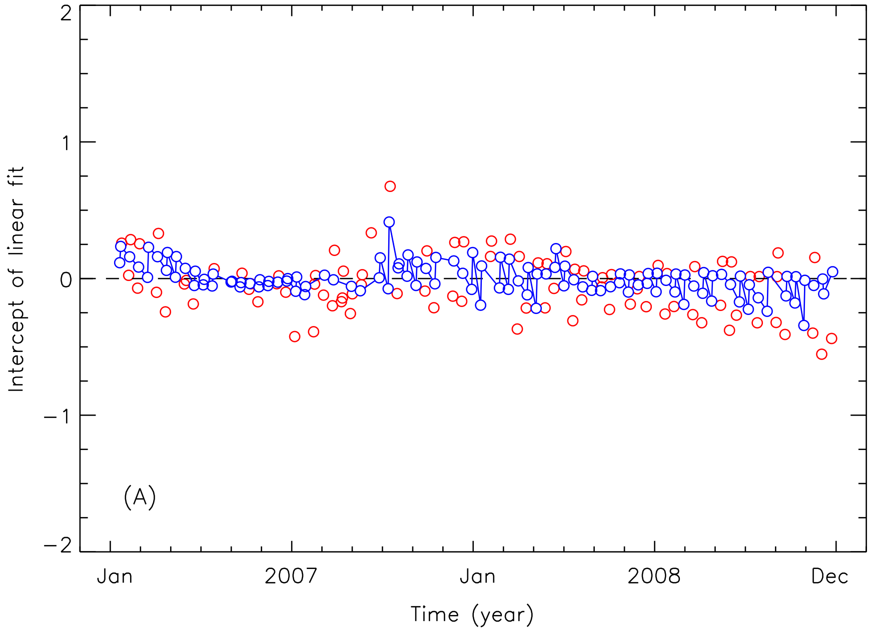

Figure 3.4: Intercept of the linear fit. The colour coding and its meaning are the same as in Fig. 3.3. The result shows that there is no clear offset found over the studied time period.

found is small and partially hidden by the noise in the data points. There appears to be a small negative trend in the time series, related to changes in the radiometric calibration of GOME-2. Note that a one index point offset can already be explained by a 2% error in the reflectance [*de Graaf et al.*, 2005].

As for the time dependence of the slopes and intercepts shown in Figs. 3.3 and 3.4, we have to conclude that – at least within the accuracy of the intercomparison – no clear systematic time dependence was found. This is expected for the slopes, because radiometric calibration errors only slightly affect the slopes, while strongly affecting the intercepts. The intercepts also show no clear time dependence, with only a slight tendency to lower values at the end of the time series. This would indicate that the GOME-2 residue has been reasonable stable over the first two years covered by the time series.

3.5 Improving the intercomparison – time series B

The statistical errors on slope and intercept, determined in the linear fitting process as illustrated in Fig. 3.2, are both on the order of 0.05. This is much less than the large variability that is actually found in Figs. 3.3 and 3.4. The much larger error is caused by a systematic error, namely the unavoidable misalignment between the SCIAMACHY and GOME-2 orbits. Figure 3.1 explains this more clearly. For the day in question, 17 October 2007, the first SCIAMACHY and GOME-2 orbits have near perfect overlap, but at the end of the day, the overlap is already quite poor. For the previous day, i.e., 16 October 2007, the situation is exactly the other way around. The best thing to do in this particular case would be to take the last ∼7 orbits of 16 October 2007, and the first ∼7 orbits of 17 October 2007, and to glue these together to form an artificial "new day". The resulting collection of orbits of this "new day" would have a much better average alignment than the collection of orbits of the two original days.

We therefore abandon the idea of letting each day start at 00:00 UTC and instead determine a careful selection of subsequent orbits for which the misalignment, in the absolute sense, is below a certain threshold. The threshold used was 1.6 degrees (in longitudes) which in normal situations yields between 14 and 17 orbits that fulfil this criterion. The artificial days created this way cover a time period of 24 hours, i.e., are spread out over the entire longitude range of the globe. Figure 3.5 shows the relative longitudinal alignment for a selection of associated SCIAMACHY and GOME-2 orbits taken from 26 and 27 February 2007. All selected orbits have an absolute relative longitudinal alignment less than 1.6 degrees.

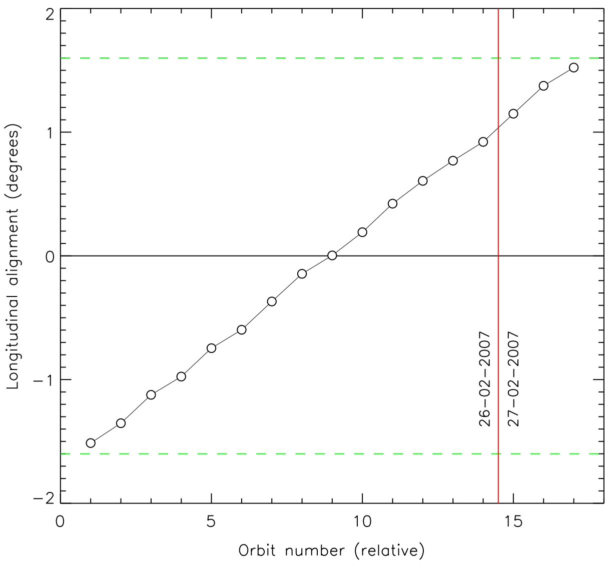

Figure 3.5: Longitudinal alignment for a selection of associated SCIAMACHY and GOME-2 orbits taken from 26 and 27 February 2007. All orbits have a longitudinal misalignment less than 1.6 degrees.

In Fig. 3.6 we present again a time series of the slope of the linear fit to the data points in the scatter plots, but now for the artificial "new days" we created. As before, the red circles indicate days for which not enough orbits were available. Narrow swath and nadir static orbits were not considered. Also compare with Fig. 3.3. Clearly, the variability in the slopes has been reduced enormously. It now amounts to roughly 0.01–0.03, which relates well to the statistical errors reported from the fitting processes. This confirms that we have removed an important error source from the intercomparison approach.

The improved accuracy, and the resulting reduced variability, now reveal that there is a seasonal variation found in the SCIAMACHY versus GOME-2 intercomparison, at least for the slope of the linear fit. The existence of a seasonal variation in the slope is not understood, and will be examined more closely in the next section. In Fig. 3.7 we present a time series of the intercept of the linear fit to the data points in the scatter plots, for the artificial "new days". The variability has been reduced considerably, and now we can clearly discern a very small downward trend in the time series of the offset.

Figure 3.8 presents the standard deviation σ of the GOME-2 versus SCIAMACHY data points in relation to the achieved linear fit. That is, if the GOME-2 AAI's are represented by the array y_i, and the SCIAMACHY AAI's are represented by the array x_i, and the best linear fit to the data can be represented by $y = mx + n$, where m is the slope and n is the intercept of the linear fit, then the standard deviation is defined as $\sigma(y_i - mx_i - n)$. The standard deviation is on the order of 0.5 index points. Note that this means that the (bias-corrected) GOME-2 AAI is therefore shown to be validated against the SCIAMACHY AAI within an accuracy ~0.5 index points. Also note that, although we went through a great deal of trouble to achieve an as accurate as possible intercomparison, there is still an inaccuracy to be attributed to the intercomparison procedure itself. That is, the "real" uncertainty in the GOME-2 AAI will be less than standard deviation of ~0.5 index points reported here, because the standard deviation also includes inaccuracies introduced by the intercomparison approach (and its intrinsic imperfections).

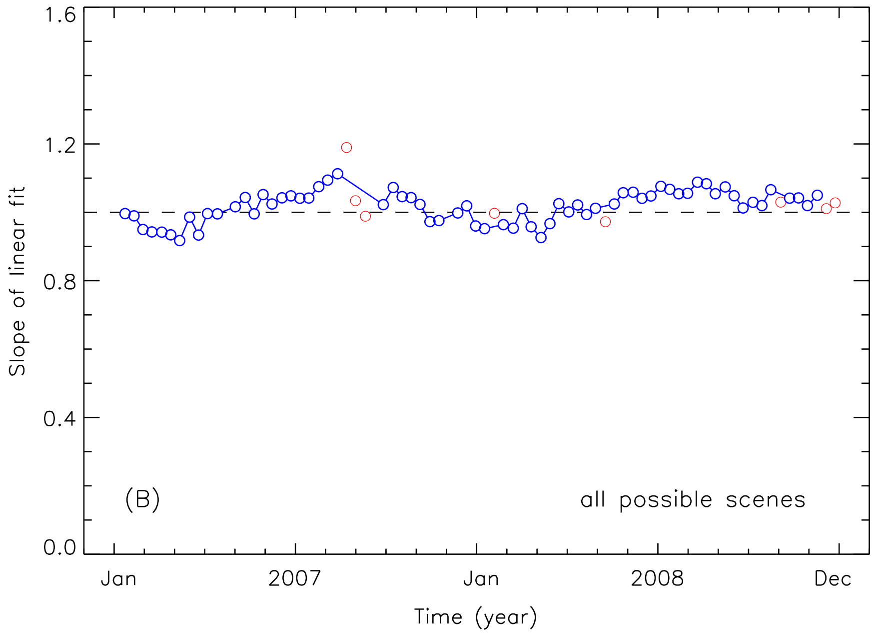

Figure 3.6: Slope of the linear fits to the (GOME-2 versus SCIAMACHY) data points as a function of time, for the new approach in which artificial days are created (approach B, see text). The red circles are believed to be unreliable: not enough orbits and/or too many GOME-2 narrow swath orbits included.

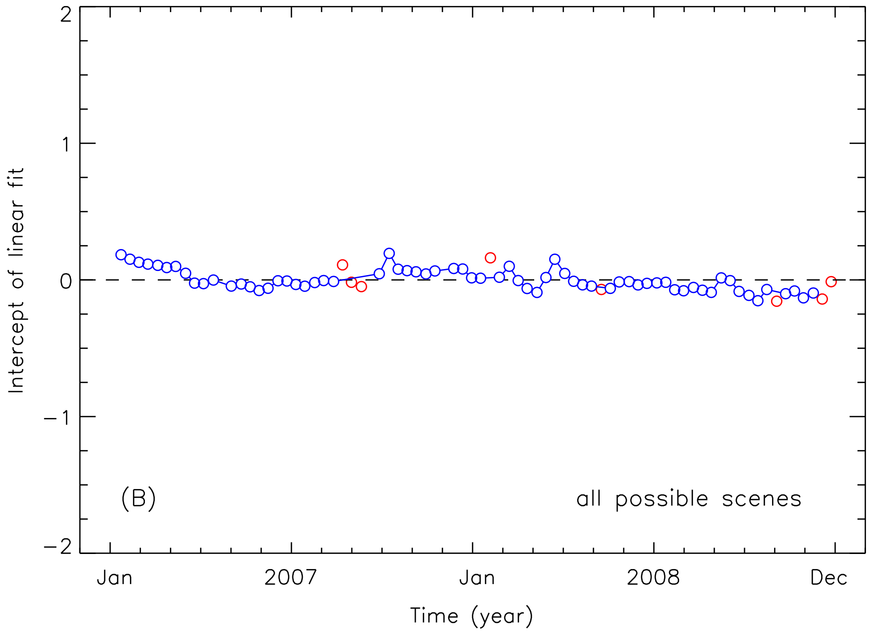

Figure 3.7: Intercept of the linear fit, for the new approach B in which artificial days are created. The colour coding and meaning is the same as in Fig. 3.6. There is only a very small offset of GOME-2 w.r.t. SCIAMACHY, changing slightly with time. The red circles are believed to be unreliable, as before.

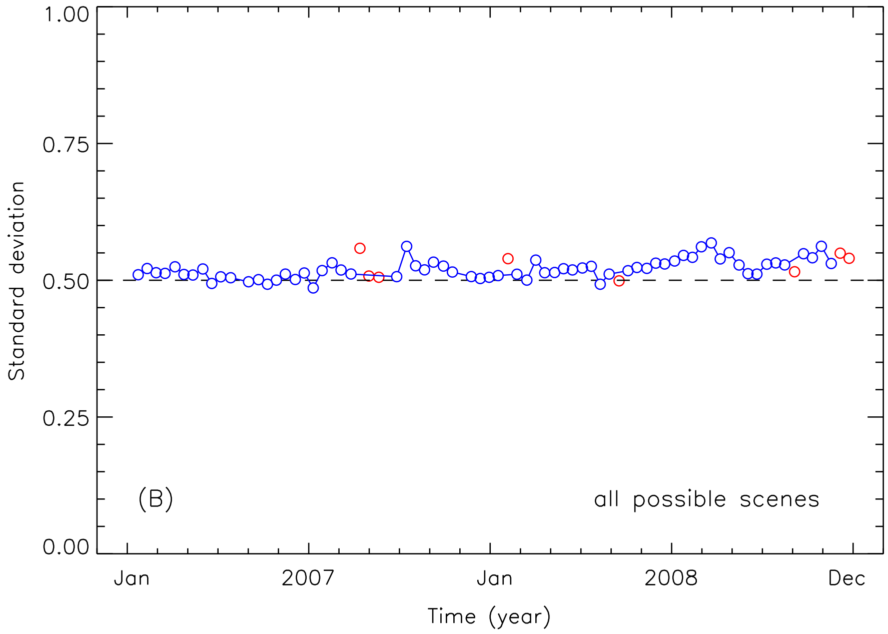

Figure 3.8: Standard deviation of the difference between linear fit and the data, for the new approach B in which artificial days are created. The standard deviation is roughly 0.5 index points, showing a slight increase with time. As before, the results for the red circles were believed to be unreliable beforehand.

3.6 Scene dependencies

In this subsection we will perform a re-analysis of the results, this time discriminating between different scene types. This is necessary, because the results of the previous section showed indications of a small seasonal variation. The presented slopes oscillated mildly around the expected one-to-one relationship. We have to exclude the possibility that the low aerosols loads in the months October to December, resulting in an absence of data with positive residues, affect the linear fit a negative way, thereby possibly creating a seasonal dependence in the time series. We discriminate between the following scene types:

1. cloudy scenes: SCIAMACHY FRESCO cloud fraction ≥ 0.1

2. clear sky scenes: SCIAMACHY FRESCO cloud fraction < 0.1 and SCIAMACHY residue < 0.5

3. aerosol loaded scenes: SCIAMACHY residue ≥ 0

The resulting time series of slope and intercept of the linear fits to the GOME-2 versus SCIAMACHY data points are shown in Figs. 3.9–3.14. Both the slope and intercept found for the subset of cloudy scenes turns out to be similar to the overall case shown in Figs. 3.6 and 3.7, where all scenes were taken into account. This is perfectly understandable, as most of the observations are in fact cloud contaminated, and cloudy scenes therefore determine the overall case.

The slopes found for the clear sky case show no clear seasonal variation, and are equal to one. Note that the retrieved intercepts are about 0.3 index points lower than the intercepts found for the cloudy case. The slopes of the aerosol loaded cases show a large scatter, due to the low number of aerosol loaded scenes and the small residue range on which to perform the fit. A seasonal variation might or might not be present, it is impossible to judge from the results presented in Fig. 3.13. The time series of the intercept shows a lot less scatter and the existence of a mild seasonal variation cannot be excluded.

To be able to study the behaviour of the aerosol loaded scenes we gather all SCIAMACHY and GOME-2 AAI measurements of the years 2007 and 2008 found using the approach described in Sect. 3.5 (method B). The biases found in Fig. 3.7 were subtracted from the GOME-2 AAI measurements, so the GOME-2 AAI's are by definition bias-corrected w.r.t. the SCIAMACHY AAI's. Figure 3.15 presents the scatter plot of GOME-2 versus SCIAMACHY of these AAI data. The blue curve is a linear fit to the data, with slope 1.03 ± 0.01. The red curve is a fit to the subset of measurements of aerosol loaded scenes. The slope is 0.97 ± 0.03, very close to one. This proves that, averaged over two years, there is indeed a near one-to-one relationship found between the SCIAMACHY and GOME-2 AAI for aerosol loaded scenes.

In conclusion, we found an indication of a small seasonal variation in the GOME-2 versus SCIAMACHY intercomparison results. It is possible that the seasonal variation is real, but it could also be artificial, i.e., an artefact of the intercomparison itself. Possibly the seasonal variation is caused by the seasonal variation in global aerosol loads, which in turn could affect the fitting results. The results of this section, however, do not provide a clear proof for this. At the same time, the intercomparison might also be affected by the fact that the SCIAMACHY and GOME-2 measurements have a slightly different solar zenith angle (see Sect. 3.3). This could lead to a seasonal variation having the right period and phase.

If the seasonal variation is real, then it is most likely a radiometric calibration problem. The algorithm of the SCIAMACHY AAI is very similar to the algorithm of the GOME-2 AAI. Note that we cannot fully exclude the possibility that SCIAMACHY causes the seasonal variation, although we should also point out that this instrument has been found to be well-calibrated w.r.t. GOME-1.

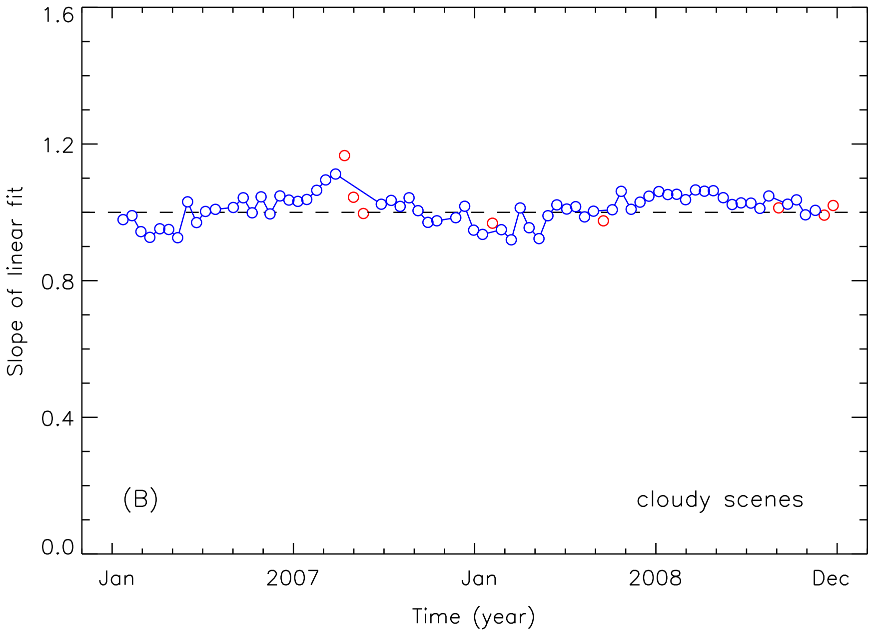

Figure 3.9: Slope of the linear fit for cloudy scenes, according to the validation method described in Sect. 3.5. The SCIAMACHY FRESCO cloud fraction was larger than 0.1 for all measurements.

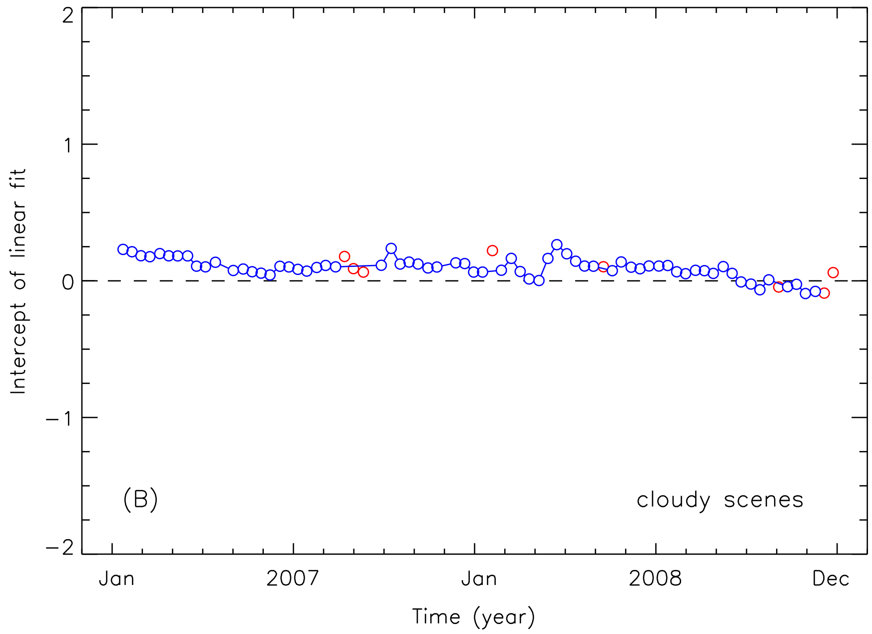

Figure 3.10: Intercept of the linear fit for cloudy scenes, according to the validation method described in Sect. 3.5. The SCIAMACHY FRESCO cloud fraction was larger than 0.1 for all measurements.

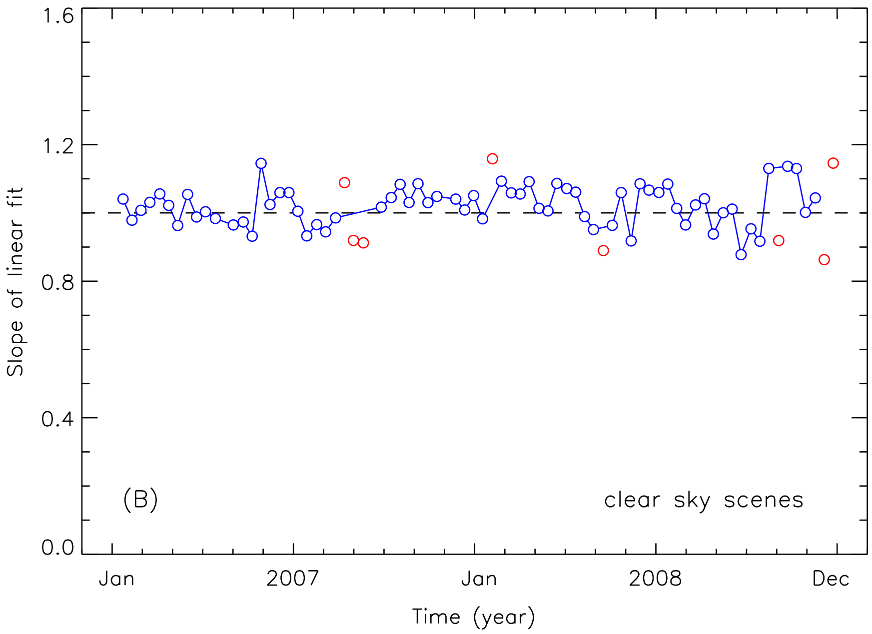

Figure 3.11: Slope of the linear fit for clear sky scenes, according to the validation method described in Sect. 3.5. FRESCO cloud fraction smaller than 0.1 and SCIAMACHY AAI smaller than 0.5.

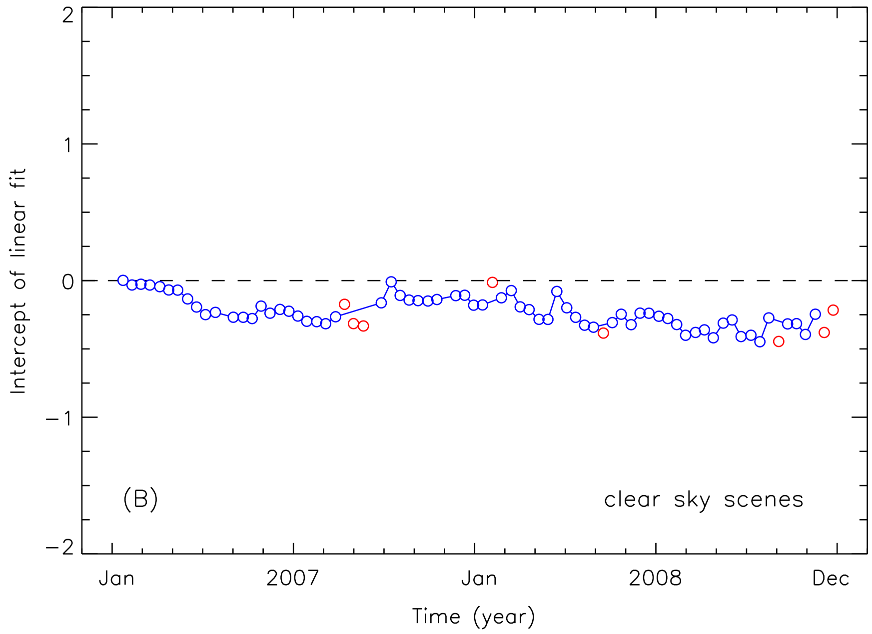

Figure 3.12: Intercept of the linear fit for clear sky scenes, according to the validation method described in Sect. 3.5. FRESCO cloud fraction smaller than 0.1 and SCIAMACHY AAI smaller than 0.5.

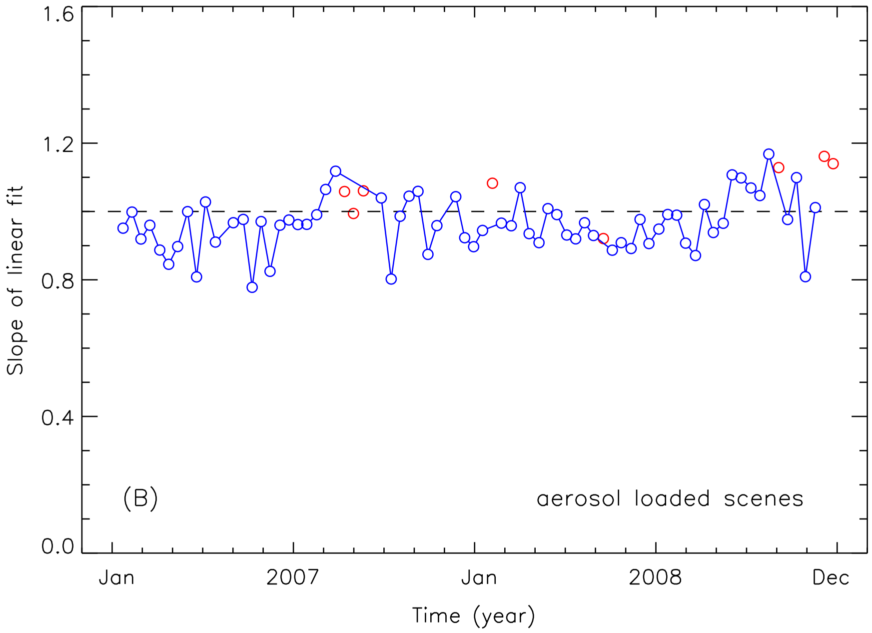

Figure 3.13: Slope of the linear fit for scenes with a sizeable aerosol load. The SCIAMACHY AAI was larger than 0.5 for all measurements. The large scatter in the data points is caused by the small number of data points having a positive residue. This is especially the case outside the aerosol season.

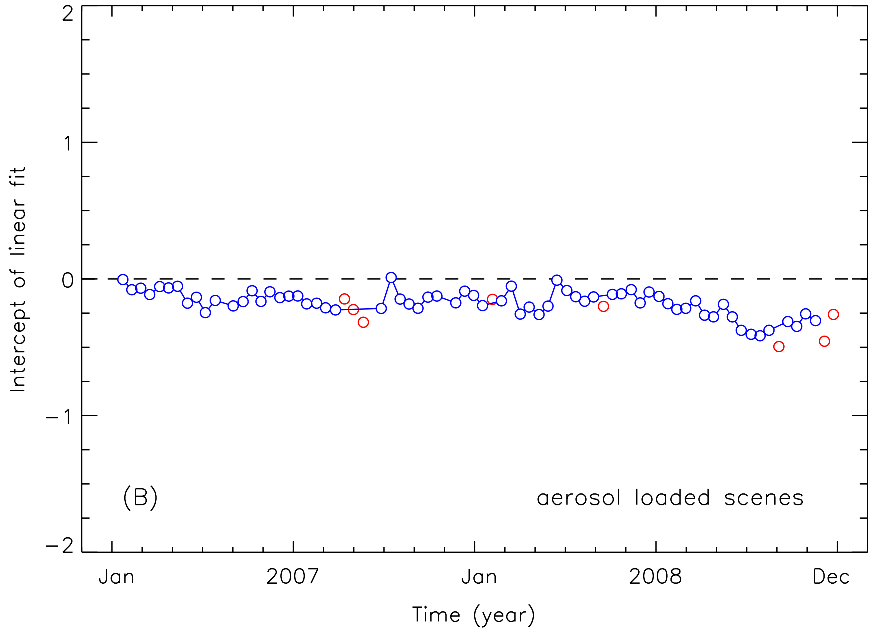

Figure 3.14: Intercept of the linear fit for scenes with a sizeable aerosol load. The SCIAMACHY AAI was larger than 0.5 for all measurements used.

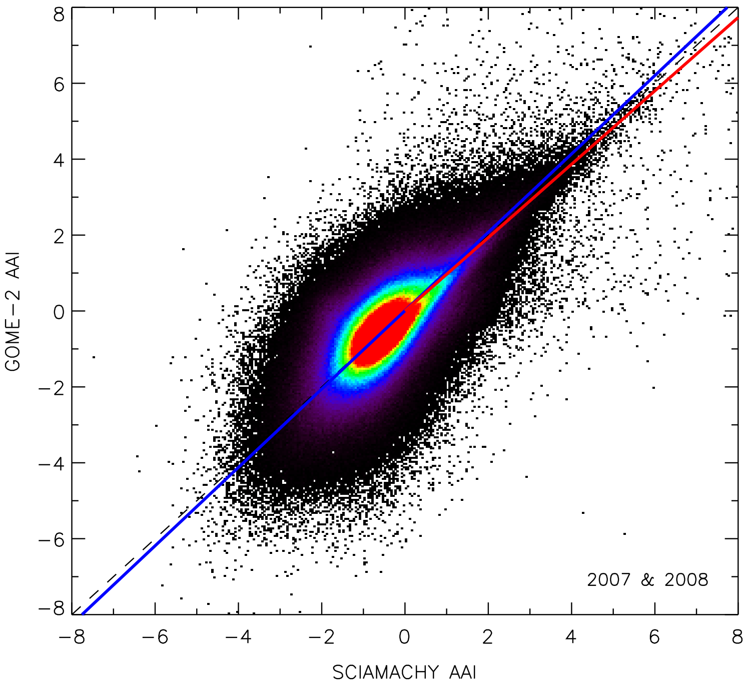

Figure 3.15: The collocated GOME-2 AAI versus the SCIAMACHY AAI, taken from all the 81 artificial days found in 2007 and 2008 for which the collocation is nearly perfect. The GOME-2 AAI's were bias-corrected. The blue curve is a linear fit to the data, with slope 1.03 ± 0.01. The red curve is a fit to the subset of measurements of aerosol loaded scenes. The slope is 0.97 ± 0.03.

3.7 Discussion of results

The results seem to indicate that there is a good correlation between the GOME-2 AAI and the SCIAMACHY AAI, which was used as a reference. The correlation is good in the sense that (i) there is a clear linear relationship between the GOME-2 AAI and the SCIAMACHY AAI, and (ii) the slope of the linear fit to the GOME-2 versus SCIAMACHY data points is close to one. On the other hand, a mild seasonal variation was found in the time series of the slope. This may be caused by the different overpass times of the two instruments. The offset between the GOME-2 AAI and the SCIAMACHY AAI was found to be small, but shows a negative trend when analysed as a function of time. This trend is most likely related to changes in the radiometric calibration (instrument degradation).

The bias-corrected uncertainty in the GOME-2 AAI was found to be ∼0.5 index point. As explained in Sect. 3.5, this is only an upper limit, because this value is also determined by the quality of the SCIAMACHY AAI and the quality of our intercomparison approach. In any case, the (bias-corrected) value of roughly 0.5 index points relates well to the target uncertainty of 0.5 index points mentioned in the O3M SAF Product Requirements Document (PRD) [*Hovila et al.*, 2009]. Using the validation technique described in this chapter, it is not possible to reach a higher accuracy for the intercomparison results, and therefore it is impossible to assess whether or not the GOME-2 AAI could reach the PRD breakthrough level of 0.2 index points. This level might perhaps be reached, but this cannot be checked with the current intercomparison technique.

Please note that by using SCIAMACHY as a reference, the results in principle only apply to residues coming from the inner part of the GOME-2 swath, i.e., observations for which the viewing zenith angle (VZA) is below ∼33°. It is also important to mention again that we made use of forward pixels only. Backscan pixels were not taken into account in the analysis, and the results therefore only apply to the GOME-2 measurements that were performed in the forward scan of the instrument.

Chapter 4

Wavelength pair

4.1 Introduction

In this chapter we present results of a study into the importance of the exact choice of the wavelength pair. We do this using the SCIAMACHY AAI retrieval code SC-AAI, which we instruct to calculate the residue for a number of wavelength pairs for real SCIAMACHY observations.

4.2 Choice of wavelength pair

To estimate the importance of the exact choice of the wavelength pair, we used real SCIAMACHY data to calculate the residues for five different situations, i.e., for five different wavelength pairs:

1. 340/380 nm, as used for a.o. SCIAMACHY and GOME-2
2. 335/380 nm, as used previously for GOME-1
3. 340/360 nm
4. 331/360 nm, as used for a.o. TOMS-Earth Probe and the NASA OMI product
5. 354/388 nm, as used for the KNMI OMI product

The simulations were performed using the SC-AAI retrieval code (version 4.1), which is also being used to calculate the SCIAMACHY AAI as found on the TEMIS website. The only differences between the five runs were in the wavelengths used. To do the analysis, Rayleigh look-up tables (LUTs) had to be generated for all seven wavelengths involved. A complete day of SCIAMACHY data was processed. The results are summarised in Fig. 4.1, where the residues resulting from wavelength pairs 2–5 are plotted on the vertical axis, versus the residues obtained with 340/380 nm wavelength pair.

Note that the sensitivity of the residue scales roughly with the distance between the wavelengths of the wavelength pair. This is clearly illustrated by the second plot (wavelength pair 340/360 nm). For the wavelength pair 331/360 nm, there is an additional problem as the residue in this case is very sensitive to the effects of ozone absorption. Although the dependence on ozone is taken into account by the retrieval code, the dependence is very large and already small uncertainties in the used ozone columns will lead to large effects. This might be the reason for the appearance of “lobes” in the third plot of Fig. 4.1.

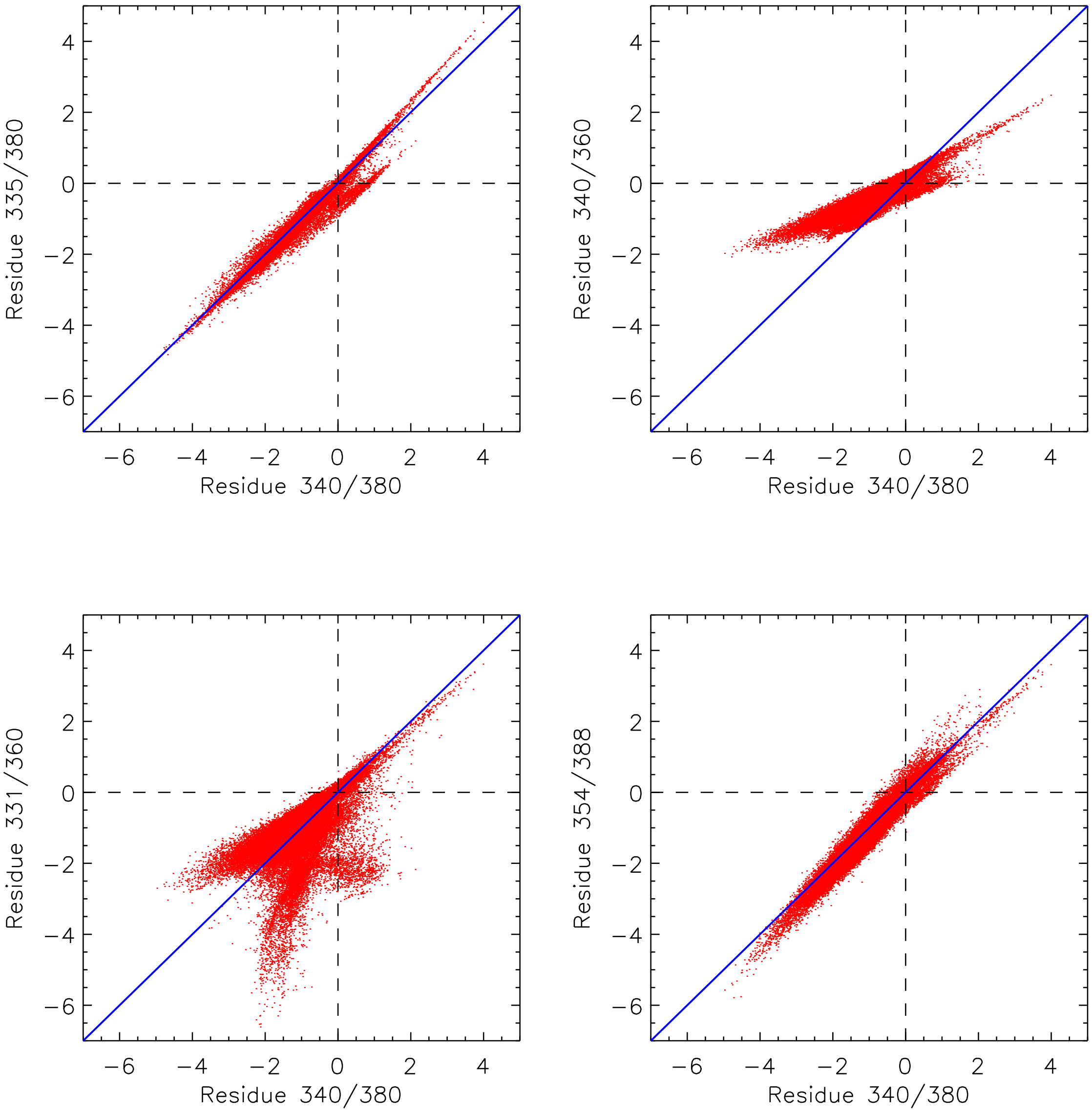

Figure 4.1: Dependence of the residue on the actual choice of the wavelength pair, simulated using real SCIAMACHY data. On the horizontal axis we plotted the residues resulting from the SCIAMACHY and GOME-2 wavelength pair 340/380 nm. On the vertical axis we present the residues of the same observations, but now based on the wavelength pairs 2–5 mentioned earlier.

Chapter 5

Statistical analyses

5.1 Short introduction

Analysing the global mean residue is a simple and robust validation technique for the AAI (see, for instance, *de Graaf et al.* [2005]; *Tilstra et al.* [2010, 2012]). The daily global mean residue, in this report, is defined as the average of all healthy residue measurements on a day located between 60°N and 60°S and having solar zenith angles below 85 degrees. This global mean turns out to be a rather stable and predictable property, which is something we can use to validate the residue/AAI.

5.2 Analysis of the global mean residue

In Fig. 5.1 we plotted the GOME-2/Metop-A global mean residue, calculated for all days of the period covered by the years 2007–2012 for which enough data were available. The daily averages are indicated by the black diamonds and were determined by averaging the residue values from all measurements between 60°N and 60°S with solar zenith angles (SZA) below 85° and being not affected by instrument anomalies or solar eclipse events. Furthermore, days with only a low coverage as well as days containing narrow swath or nadir static orbits were removed from the time series shown in Fig. 5.1.

The arrangement of the data points suggests the presence of a seasonal cycle in at least the last part of the time series. A similar seasonal cycle was found in the GOME-1 global mean residue [*de Graaf et al.*, 2005; *Tilstra et al.*, 2010]. This seasonal cycle is for the largest part a real one. That is, globally seen, there are more UV-absorbing aerosols (desert dust aerosol and biomass burning aerosol) in the months MAY–AUG than there are in the months OCT–JAN. This is clear from many publications on these types of aerosols. Note that the residue is strongly dependent on the exact scattering geometry. For that reason, for a specific region on the globe, there is a seasonal variation caused by the changing solar position. The idea behind the global mean residue is that these effects cancel out for the largest part when we consider a region which is symmetrical around the equator, and which covers a sufficiently large latitude range. Only for a small range of latitudes the seasonal variation does not cancel out. The seasonal cycle is a "real" one, and the GOME-2 data should reflect this seasonal cycle in the global mean residue.

The seasonal variation that was found for GOME-1 was parameterised using the method outlined in *de Graaf et al.* [2005] and based on results presented in *Tilstra et al.* [2010]. The sinusoidal parameterisation is presented in Fig. 5.1 by the red curve. Note that the GOME-1 global mean residue assumes a mean value of around -0.7, which is a bit lower than the mean value of -0.3 we now find for GOME-2. However, the GOME-1 swath width is only half of that of GOME-2. The green circles represent the GOME-2 global mean residue based on the inner “GOME-1” part of the GOME-2 swath. This explains part of the discrepancy that was found. For the GOME-2 global mean residue, we assume that the following equation can reasonably describe the temporal variation found in the data points:

$$y_0 = a_0 + a_1 t + a_2 \sin(2\pi t + a_3) \tag{5.1}$$

This relationship basically assumes a seasonal cycle on top of a linear trend of the form

$$y_1 = a_0 + a_1 t \tag{5.2}$$

In Fig. 5.1, the fit of Eq. 5.1 to the GOME-2 data after August 2007 is given by the solid blue curve. The curve is extended into the non-fitted area by a dashed blue curve. The red line represents Eq. 5.2. For the fit parameters, we found $a_0 = 458.9$, $a_1 = -0.2287$, $a_2 = 0.1032$, and $a_3 = -0.301$. The agreement with the result found for GOME-1 is good, but only for data after August 2007. Before that point in time, there appears to be an additional signal in the global mean residue, possibly related to radiometric changes.

Also present in Fig. 5.1 are five vertical lines. Jumps in the global mean residue occur at the dates associated with these lines. The first vertical line corresponds to 11 March 2008. On this day, a new PMD band definition (v3.1) was uploaded to the satellite instrument. As a result, the global mean residue jumped up by ~0.2 index points. The second line corresponds to 18 August 2009, when a software change (from v4.2 to v4.3) occurred in the GOME-2 data processor. The global mean residue jumped down by ~0.2 index points. The third line corresponds to 9 September 2009, right in the middle of a throughput test of the GOME-2 instrument. The direct effect of this throughput test was very small.

We can conclude that there is a indeed a seasonal cycle present in the GOME-2 data, accompanied by a downward trend which is for sure caused by the effects of instrument degradation, and features before August 2007 which seem to be related to changes in instrument response. The exact origin of the effects and features we describe here are not yet completely understood. Note that the downward trend, given by

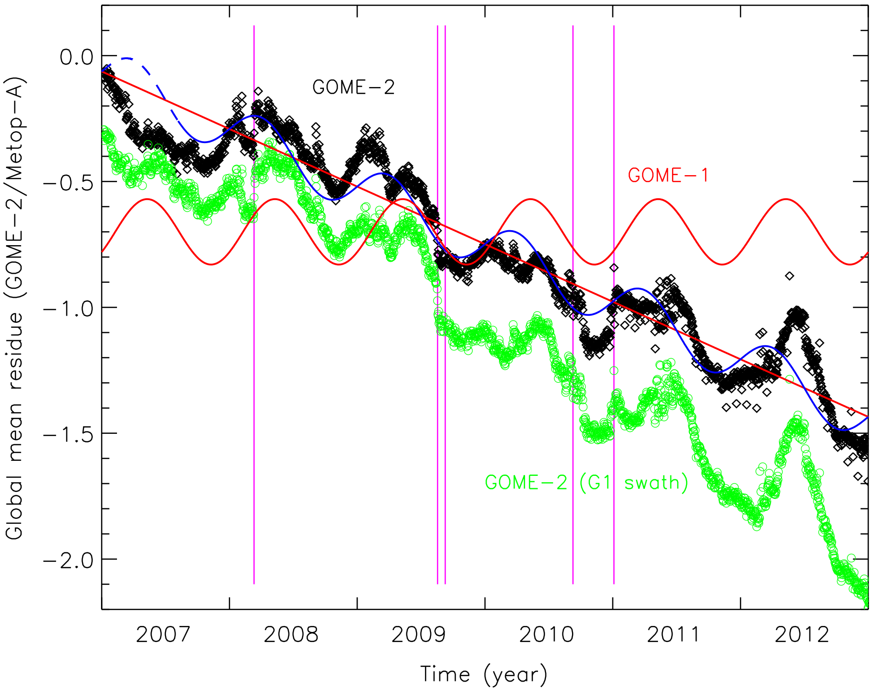

Figure 5.1: Global mean residue observed by GOME-2/Metop-A versus the time for the years 2007–2012 (black diamonds). The green circles also represent the GOME-2 global mean residue, but now based on only the inner “GOME-1” part of the swath. The blue curve is a fit of Eq. 5.1 to the GOME-2 global mean. The red line represent Eq. 5.2. Clearly, the data show a seasonal cycle, as well as a downward trend. The seasonal cycle reported for GOME-1 by *de Graaf et al.* [2005] is also indicated, for comparison.

the fitting coefficient a_1, is at the moment still modest. On the other hand, the accumulated effect after six years of instrument degradation is rather large, and starting to become problematic.

5.3 Dependence of global mean residue on scanner angle

In this section we present results for the global mean residue for individual positions of the scanner mirror. For observations between 60°N and 60°S, the integration time is 187.5 ms, leading to 32 measurements per scan, of which the last 8 are backscan measurements. Despite the fact that the number of measurements over which is averaged decreases by a factor of 32 when we restrict ourselves to individual scanner mirror positions, we still end up with a statistical property which is fit for quantitative analysis.

5.3.1 Metop-A

In Fig. 5.2 we present the GOME-2/Metop-A daily global mean residue versus time for all forward scan mirror positions. There are 24 measurements inside each forward GOME-2 scan, resulting in 24 time series, each with their own colour and labelled by their own "IndexInScan" number. The general behaviour for each of the scanner mirror positions is similar to that presented in Fig. 5.1, but there is also a clear difference in offset. Also, the value of the global mean of one scanner angle relative to those of the other scanner angles is varying. This is a bit more clearly shown by Fig. 5.3, which differs from Fig. 5.2 in the sense that only data for a selection of scan mirror positions is plotted. The westernmost scanner mirror position (given in black) shows significantly different temporal behaviour than the easternmost scanner mirror position (given in dark blue). More importantly, at the start of the time series, the easternmost and westernmost scanner mirror positions show exactly the same value for the global mean residue. But exactly four years later, the difference has increased to roughly 3.0 index points.

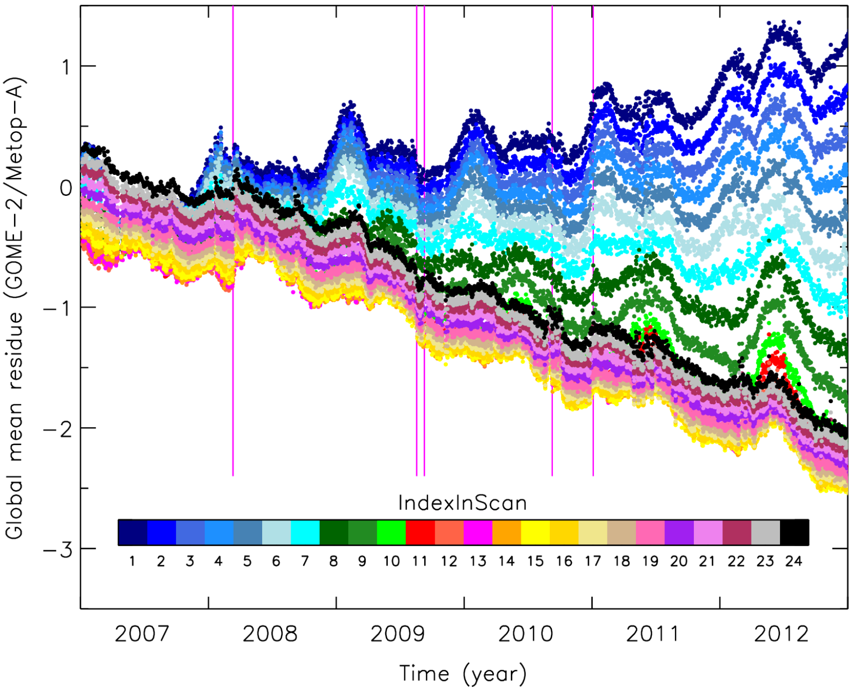

Figure 5.2: Daily global mean residue for all 24 forward scan mirror positions inside the GOME-2 swath plotted versus the time. The colours relate to the "IndexInScan" number, as indicated by the colour bar. There is a clear dependence on scanner angle next to the temporal variation already shown in Fig. 5.1.

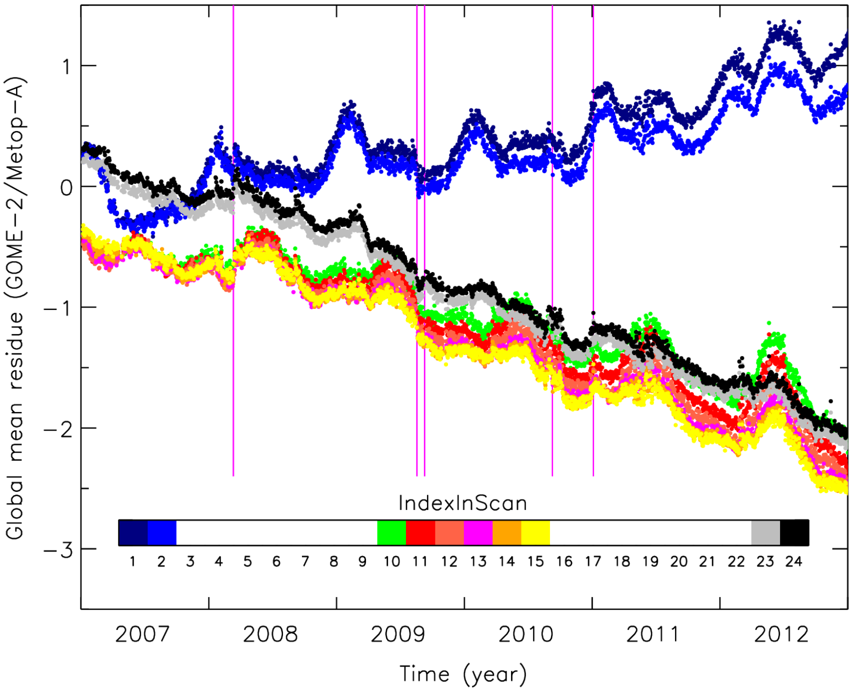

Figure 5.3: Daily global mean residue versus time for a selection of the 24 forward scan mirror positions inside the GOME-2 swath. Compare with Fig. 5.2. Clearly, the different temporal behaviour of the global mean residue for the different scan mirror positions is pointing to a growing scan-angle dependence.

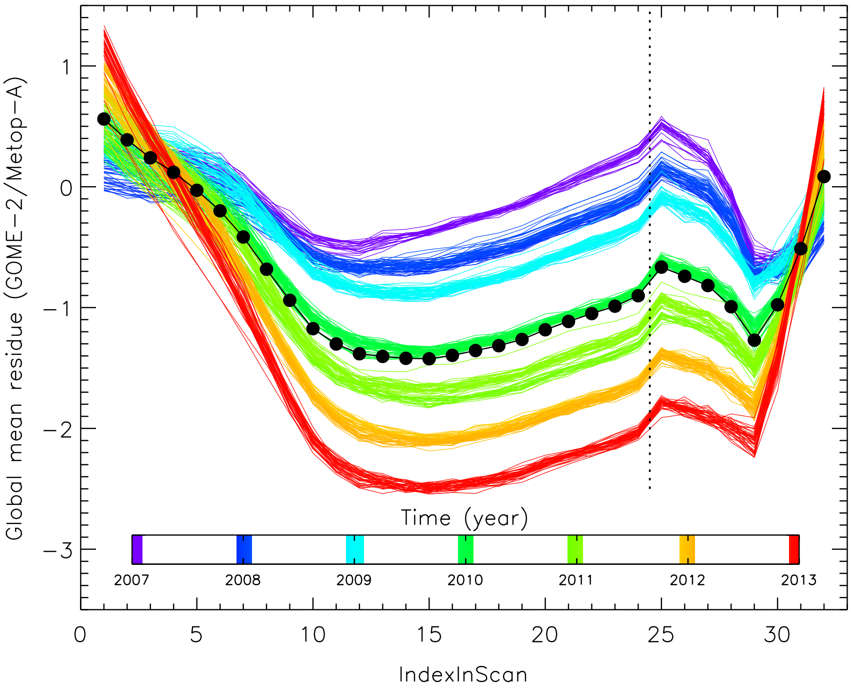

Figure 5.4: Global mean residue as a function of scanner mirror position, for all available days. The colours can be related to the actual date using the colour bar. The circles represent the global mean residue over all days. The vertical dotted line illustrates the westernmost scanner angle position.

To study this phenomenon more clearly, we present in Fig. 5.4 the same collection of data, but plotted in a different way. On the vertical axis we present again the global mean residue, but on the horizontal axis we now plot the "IndexInScan" number. This number in this case goes up to 32, because we included the backscan results as well. The backscan positions are separated from the forward scan positions by the vertical dotted line. The colours that are used can be related to the actual date using the colour bar. Additionally, the string of black circles indicates an average taken over all available data.

The global mean residue follows the expected behaviour, apart from an offset w.r.t. the GOME-1 global mean of -0.7, but Fig. 5.4 also shows that there seems to be a time dependent shift in the global mean residue as a function of scanner angle. For the forward scan part, the scanner angle dependence is roughly symmetrical in the exact nadir viewing position at the (virtual) IndexInScan position of 12.5. Note that instruments like GOME-1 and SCIAMACHY have much smaller swaths, which basically cover the IndexInScan range 7–18. In this range, the residue is only slightly dependent on scanner angle. For GOME-2, however, the residue increases at the edges of the swath by roughly 0.7 index points.

The backscan pixels show strange (unexpected) behaviour: (i) the difference in global mean residue between the middle and the edges of the swath is larger (and not smaller, as expected), (ii) the global mean residue is not symmetrical w.r.t. the exact nadir position at IndexInScan equal to 28.5, (iii) the global mean residues at the two swath edges are not equal (not even at the start of the mission). This behaviour is perhaps caused by what is known as the spatial aliasing effect [*Munro and Eisinger*, 2006]. Because of the finite read-out time of the detector pixels of the main science channels, the starting time of the accumulation time interval by the individual detector pixels is not the same. For instance, when the

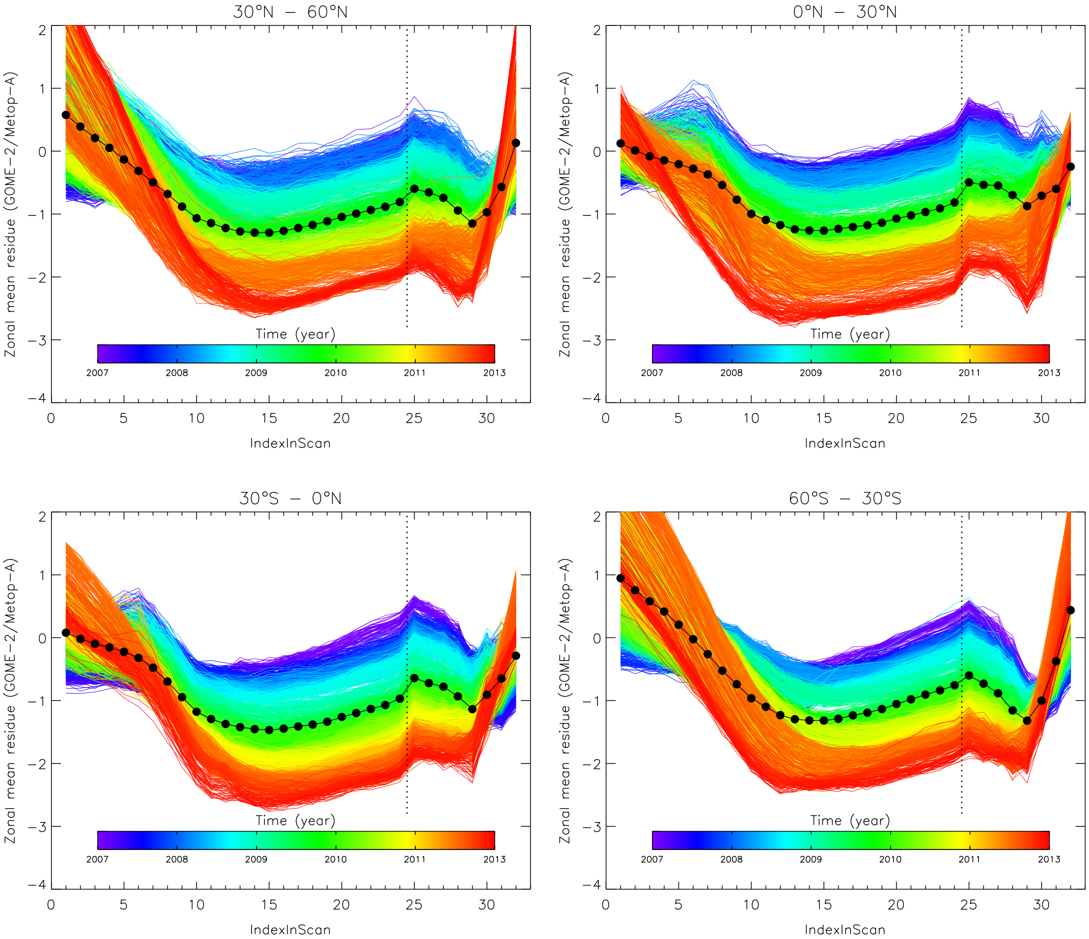

Figure 5.5: Zonal mean residue as a function of scanner mirror positions, for the four latitude bands indicated. Notice the much stronger time dependence for the eastern pixels as compared to Fig. 5.4.

first detector pixel of spectral channel 3 starts accumulating the incoming radiation, the last detector pixel of the spectral channel starts doing the same exactly 46.875 ms later. For spectral channel 2, it is the other way around, and the first detector pixel is read out 46.875 ms later than the last detector pixel. For the two wavelengths 340 and 380 nm, both residing in spectral channel 2, the time difference is roughly half of that, i.e., on the order of 1/8th of the integration time. For the backscan pixels, the effect is three times as large because of the three times larger scan speed of the scanner mirror, and in the opposite direction.

To also gain some more insight in the latitudinal dependence of the scanner angle dependence of the global mean residue, we present in Fig. 5.5 four similar plots, but now the averaging was performed over four distinct latitude bands. The plots present the zonal mean residue over a latitude range of 30°. This results in a somewhat higher "noise", but also results in a time dependence caused by the changing solar position throughout the year. (When considering the global mean, this effect is more or less absent). Note that the effect that the changing solar position has on the single scattering angle Θ is the largest for eastern pixels. The four plots confirm what was already reported after visual inspection of global maps of the residue, namely that the residues at the eastern side of the swath shows high values near the poles, but only in certain parts of the year. This seems to be a geometric property of the residue.

5.3.2 Metop-B

The time range covered by GOME-2 on Metop-B is too small for a meaningful analysis of the global mean residue as a function of time. However, the global mean residue as a function of scanner mirror position, presented in Fig. 5.6, clearly shows that the GOME-2/Metop-B residue is in good agreement with the GOME-2/Metop-A residue at the start of the Metop-A mission in January 2007. Data from the period between 4 and 12 March 2013 were filtered out, because in this period Metop-B operated in a 960 km wide swath mode. Compare with Fig. 5.4 and mind the different range of the vertical axis. There appears to be a small positive offset of ~0.3 index points in the GOME-2/Metop-B residue compared to the GOME-2/Metop-A residue. This follows not only from Fig. 5.6 but also from more detailed analyses.

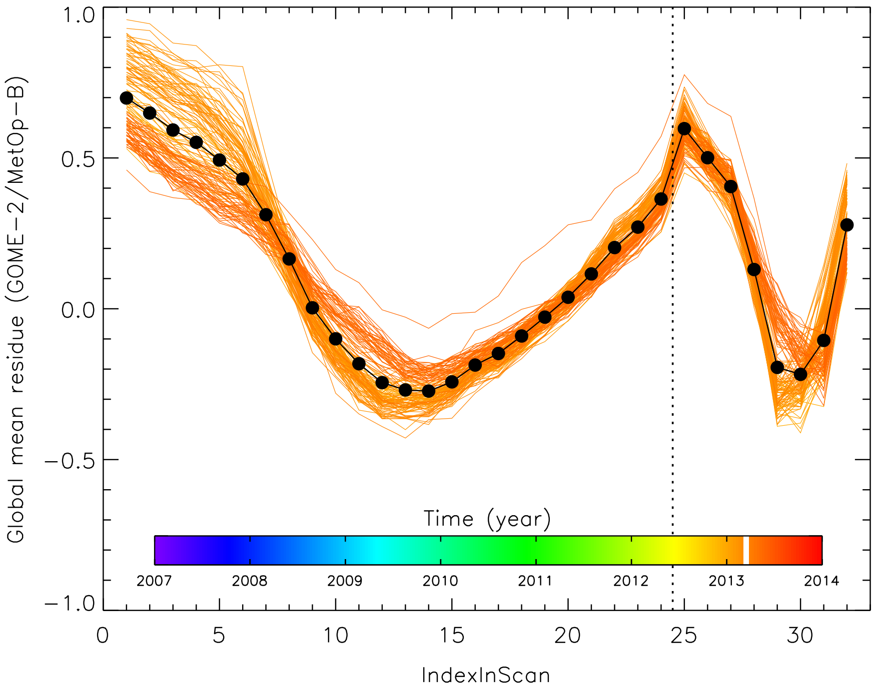

Figure 5.6: Global mean residue measured by GOME-2 on the Metop-B platform as a function of scanner mirror position. Data between 4 and 12 March 2013 were filtered out. Also compare with Fig. 5.4.

5.4 Other statistical characteristics

In this section we will present the results from other statistical analyses. We analysed the data set available for one entire month for July 2008 (GOME-2/Metop-A) and January 2013 (GOME-2/Metop-B).

5.4.1 Metop-A

The data are from the month July 2008, comprising a total of 433 orbits. In Fig. 5.7, we present the histogram of all the residues measured by GOME-2 in that month. The distribution is symmetrical, as we would intuitively expect. The mean value of the GOME-2/Metop-A AAI has a bias -0.331 ± 0.933.

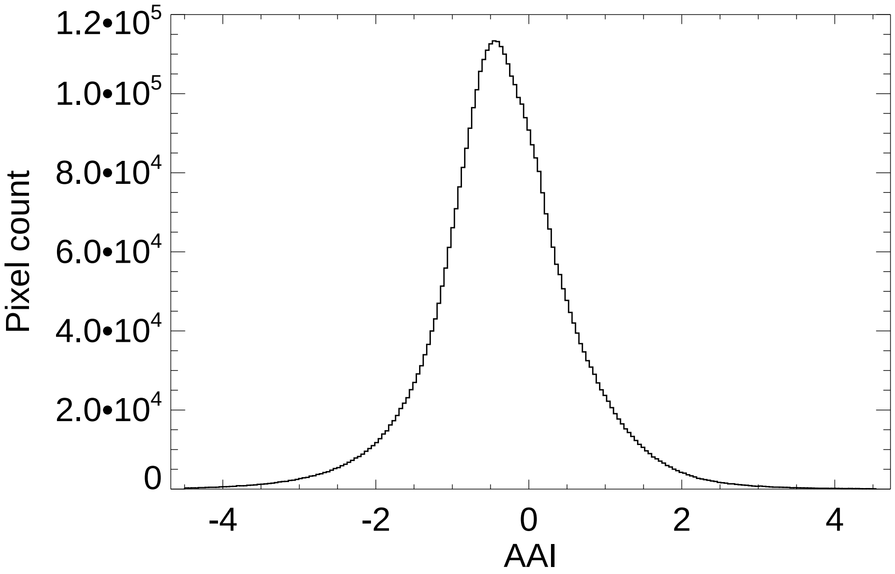

Figure 5.7: Histogram of all the AAI (residue) values measured by GOME-2 in July 2008. The distribution is highly symmetrical, as expected, and as it should be. The mean value is -0.331 ± 0.933.

In Fig. 5.8 we present the scatter density plot of the distribution of the AAI against the "IndexInScan" number. Only measurements from the forward scan are considered in the remainder of this section. In the left plot we used a logarithmic scale, on the right a linear scale is used. The results are very comparable to the results that we presented earlier in Fig. 5.4.

In Fig. 5.9 we did the same for the solar zenith angle (SZA). Here do not find a very clear relationship between AAI and SZA, which is a satisfying result. In Figs. 5.10 and 5.11 we present the results for the solar azimuth angle (SAA) and the relative azimuth angle (RelAA), both without a very clear relationship to the AAI. Figure 5.12, in which we relate the AAI to the single scattering angle (ScatAngle) is interesting, though, because there appears to be a very small dependence above scattering angles of 100°, but a large dependence below scattering angles of 100°. The latter scattering angles are found at high latitudes, near the poles. This relationship between AAI and scattering angle needs to be checked.

Figure 5.13 shows that there is no real correlation between ozone column and AAI. If there would have been a correlation, then this would have pointed to errors, or an insufficient knowledge of the ozone column used. In Fig. 5.14, we check for a dependence on surface height. There does not appear to be such a correlation, which is indeed the preferred behaviour.

Finally, in Fig. 5.15 we present the distribution of the AAI against the latitude. Here we can clearly identify the desert dust events (around latitudes of 20°N) and the biomass burning events (around latitudes of 10°S). In conclusion, the AAI behaves as it should do, with the exception of the behaviour for scattering angles below 100°. This behaviour may be suspicious and needs to be analysed.

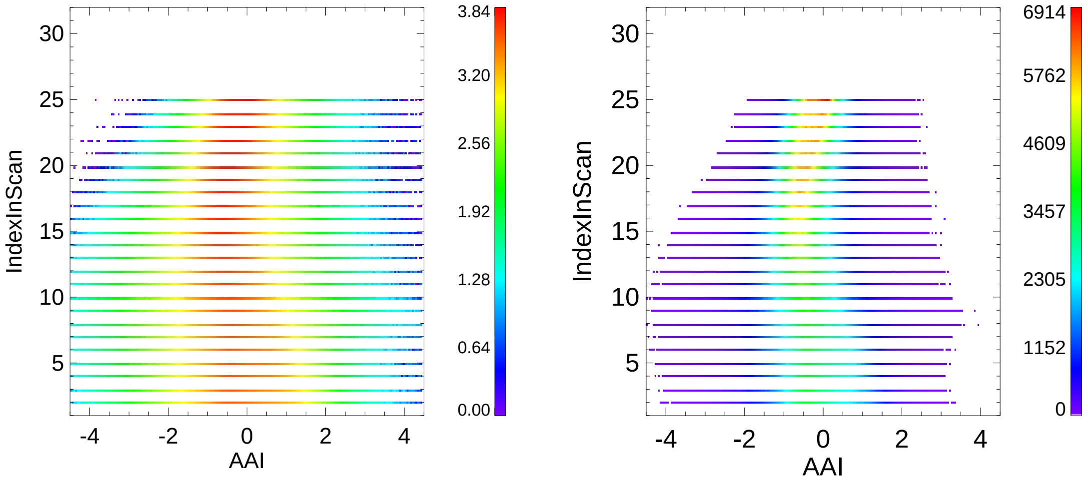

Figure 5.8: GOME-2/Metop-A: Scatter density plot of the distribution of the AAI against the IndexInScan on a logarithmic colour scale (left) and a linear colour scale (right).

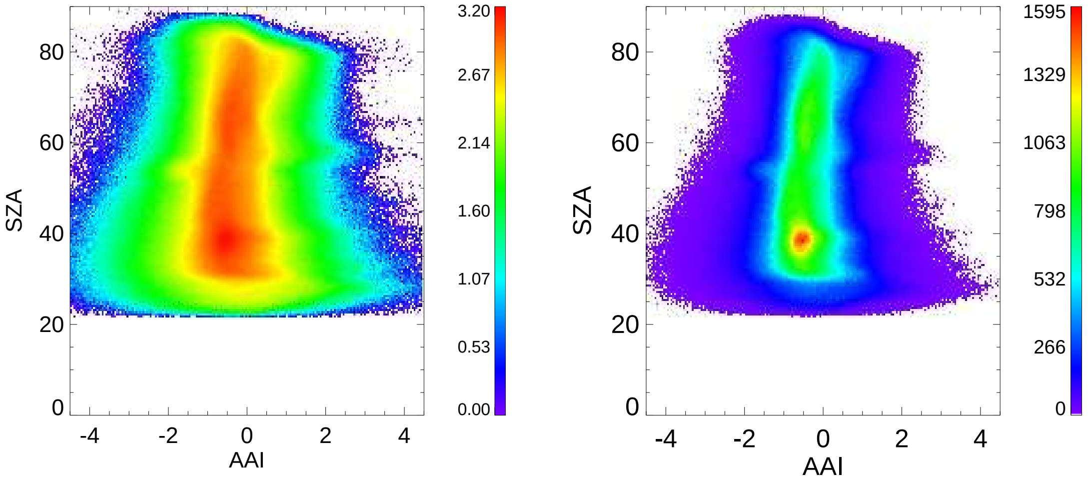

Figure 5.9: GOME-2/Metop-A: Scatter density plot of the distribution of the AAI against the solar zenith angle (SZA) on a logarithmic colour scale (left) and a linear colour scale (right).

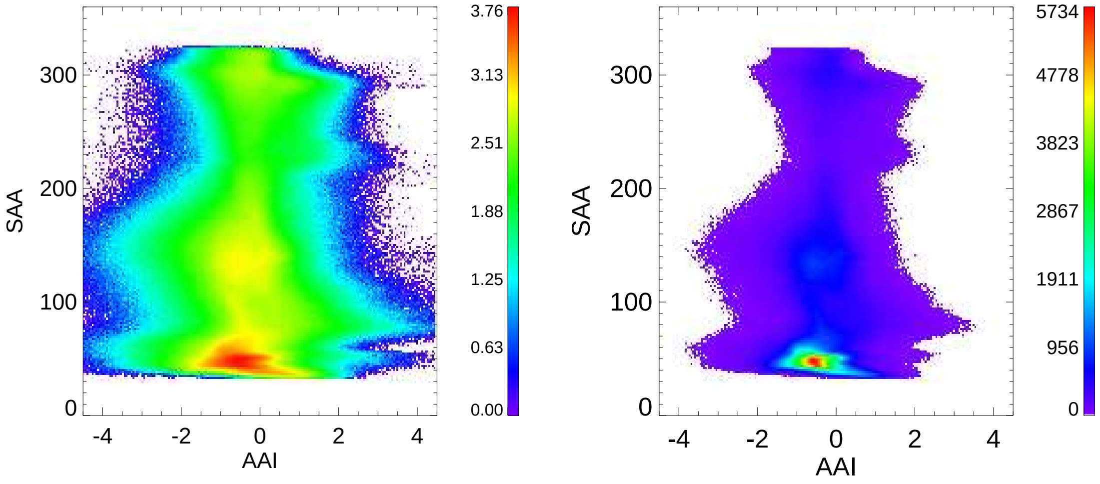

Figure 5.10: GOME-2/Metop-A: Scatter density plot of the distribution of the AAI against the solar azimuth angle (SAA) on a logarithmic colour scale (left) and a linear colour scale (right).

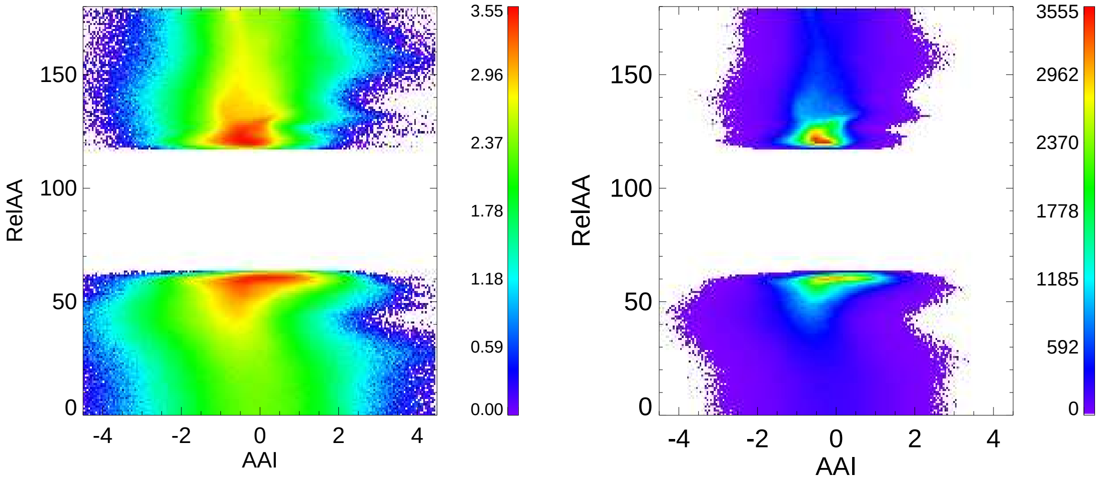

Figure 5.11: GOME-2/Metop-A: Scatter density plot of the distribution of the AAI against the relative azimuth angle (RelAA) on a logarithmic colour scale (left) and a linear colour scale (right).

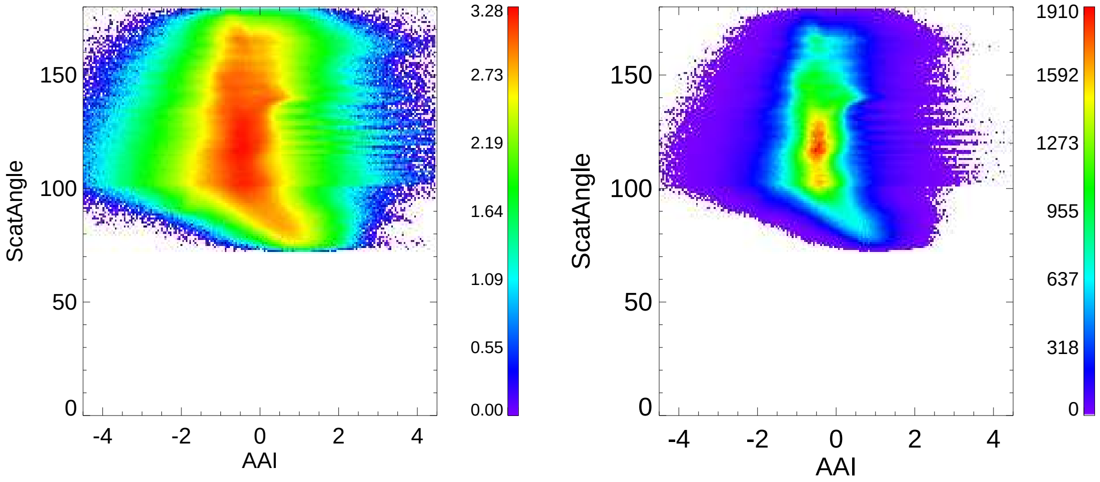

Figure 5.12: GOME-2/Metop-A: Scatter density plot of the distribution of the AAI against the single scattering angle (ScatAngle) on a logarithmic colour scale (left) and a linear colour scale (right).

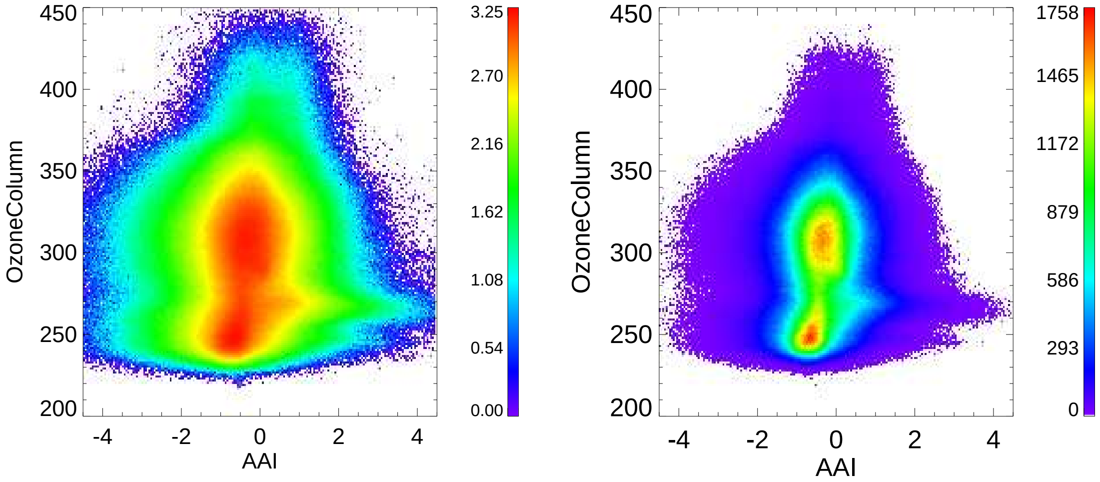

Figure 5.13: GOME-2/Metop-A: Scatter density plot of the distribution of the AAI against the ozone column on a logarithmic colour scale (left) and a linear colour scale (right).

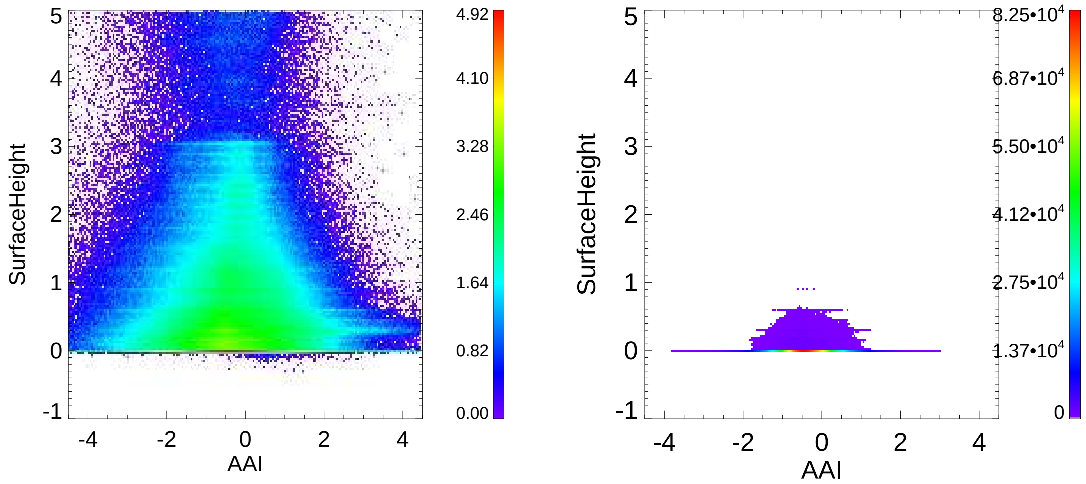

Figure 5.14: GOME-2/Metop-A: Scatter density plot of the distribution of the AAI against the surface height on a logarithmic colour scale (left) and a linear colour scale (right).

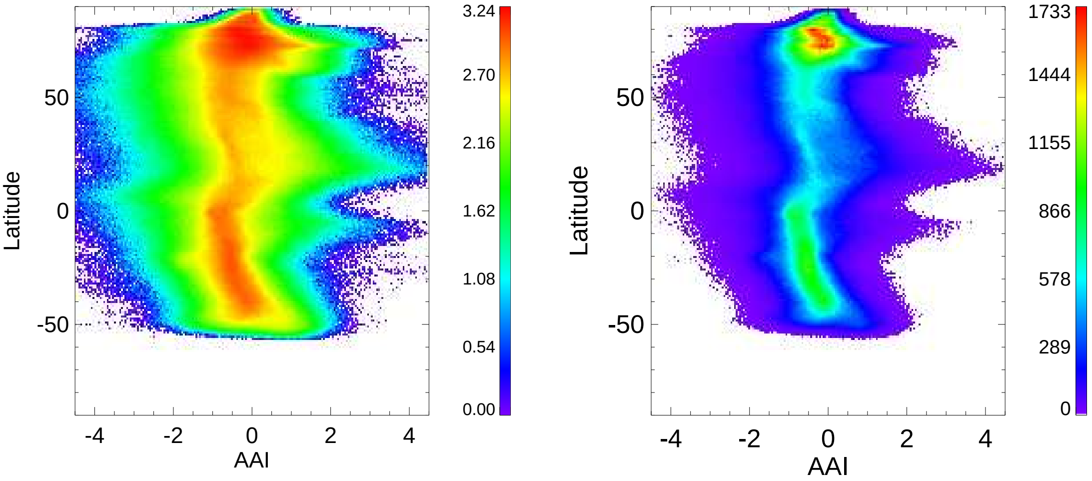

Figure 5.15: GOME-2/Metop-A: Scatter density plot of the distribution of the AAI against the latitude on a logarithmic colour scale (left) and a linear colour scale (right).

5.4.2 Metop-B

The data are from the month January 2013. In Fig. 5.16, we present the histogram of all the residues measured by GOME-2 in this month. The mean value of the GOME-2/Metop-B AAI is -0.0153 ± 0.844. This is somewhat higher than the mean value found in section 5.4.1 for GOME-2/Metop-A, but this may be due to the fact that for Metop-A a different month was selected.

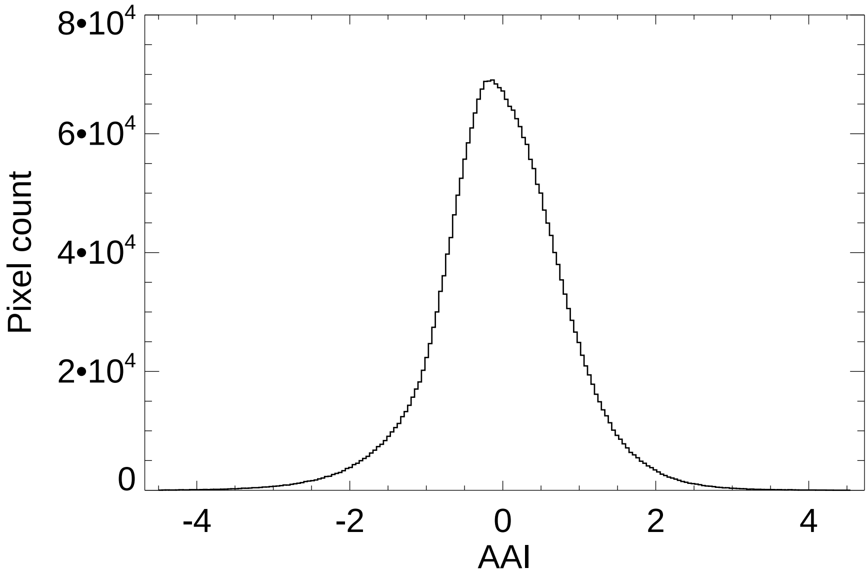

Figure 5.16: Histogram of all the AAI (residue) values measured by GOME-2/Metop-B in January 2013. The mean value is -0.0153 ± 0.844.

In Figs. 5.17–5.24 we present the same results also shown in Figs. 5.8–5.15, but now for GOME-2 on the Metop-B platform. The results are very similar. Differences are mainly caused by the difference in scattering geometry caused by the fact that different months were studied. All in all, we can conclude that the GOME-2 instruments on both Metop platforms provide consistent AAI data.

5.5 Discussion of results

The general behaviour and quality of the GOME-2 AAI measured from both the Metop-A and Metop-B platforms is good. For the GOME-2/Metop-A global mean residue we found a value of -0.3 ± 0.1 which is higher than the value of -0.7 found for GOME-1 (see section 5.2). Part of this offset can be explained by the larger swath width of GOME-2. Taking this into account still leaves a small offset of $\sim$0.2 index points unexplained. For the GOME-2/Metop-B global mean residue we found similar results, although a small offset of $\sim$0.3 index points w.r.t. GOME-2/Metop-A does exist (see section 5.3.2).

For the GOME-2/Metop-A AAI, instrument degradation of Metop-A has become more and more influential over the last years. We found that the instrument degradation is scan-angle dependent, leading to an east/west bias of $\sim$3 index points after the first six years after launch. For the GOME-2/Metop-B AAI, instrument degradation of Metop-B is at the moment not a very severe issue.

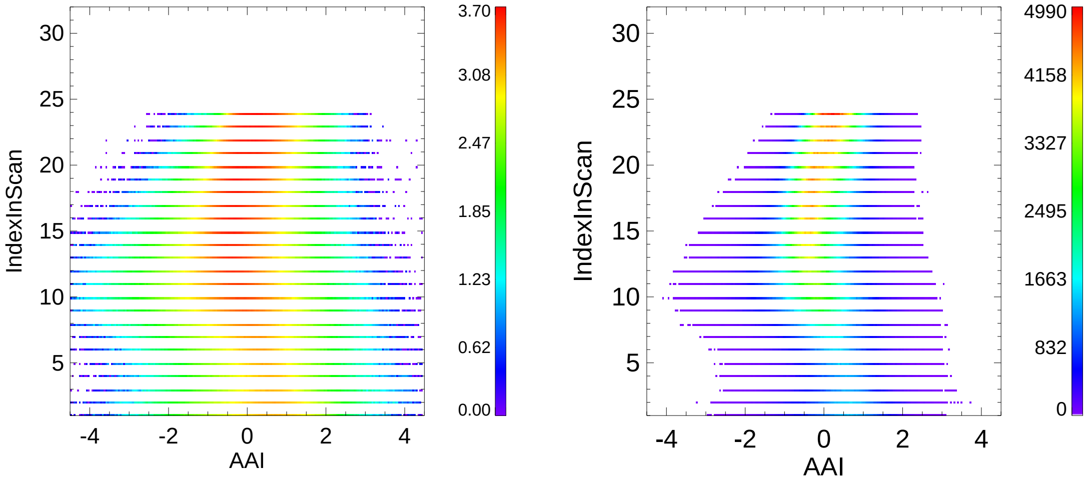

Figure 5.17: GOME-2/Metop-B: Scatter density plot of the distribution of the AAI against the IndexInScan on a logarithmic colour scale (left) and a linear colour scale (right).

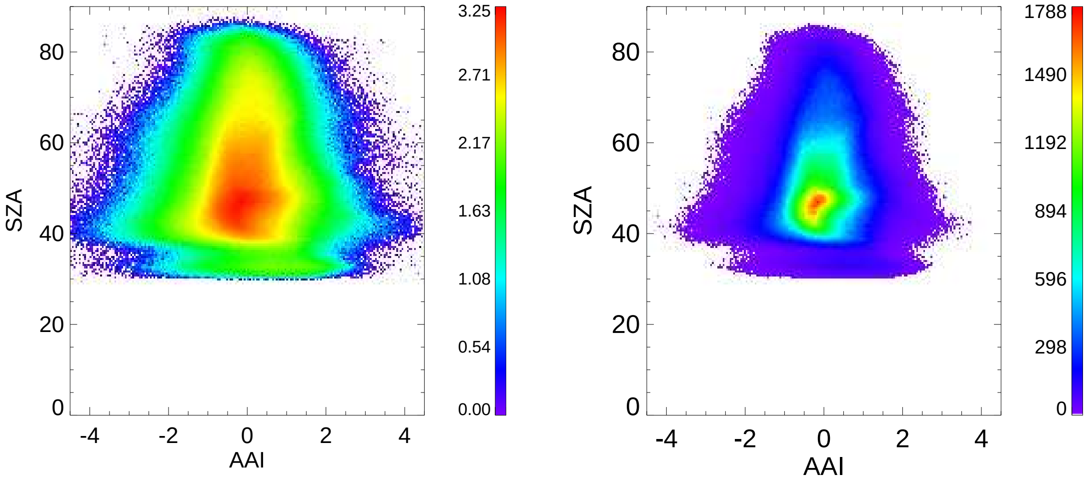

Figure 5.18: GOME-2/Metop-B: Scatter density plot of the distribution of the AAI against the solar zenith angle (SZA) on a logarithmic colour scale (left) and a linear colour scale (right).

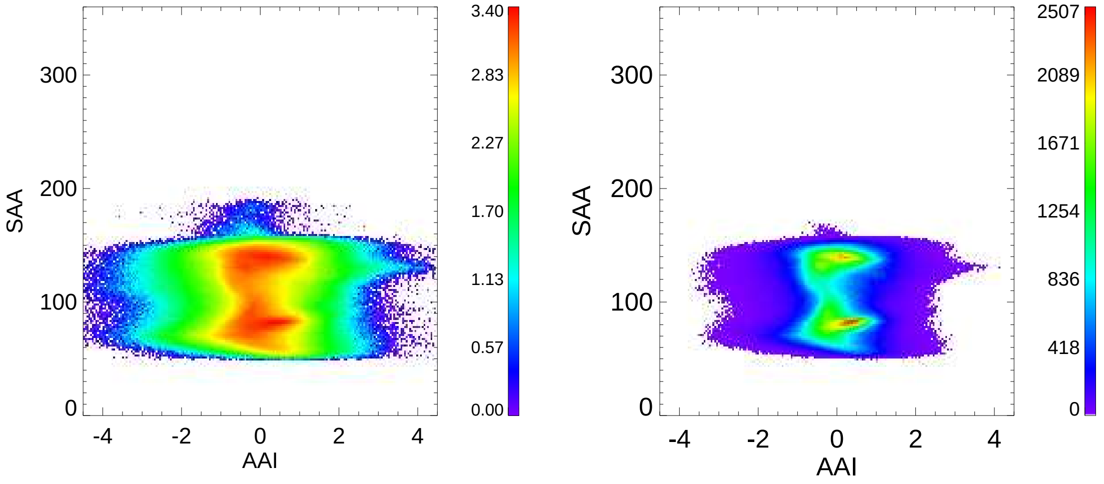

Figure 5.19: GOME-2/Metop-B: Scatter density plot of the distribution of the AAI against the solar azimuth angle (SAA) on a logarithmic colour scale (left) and a linear colour scale (right).

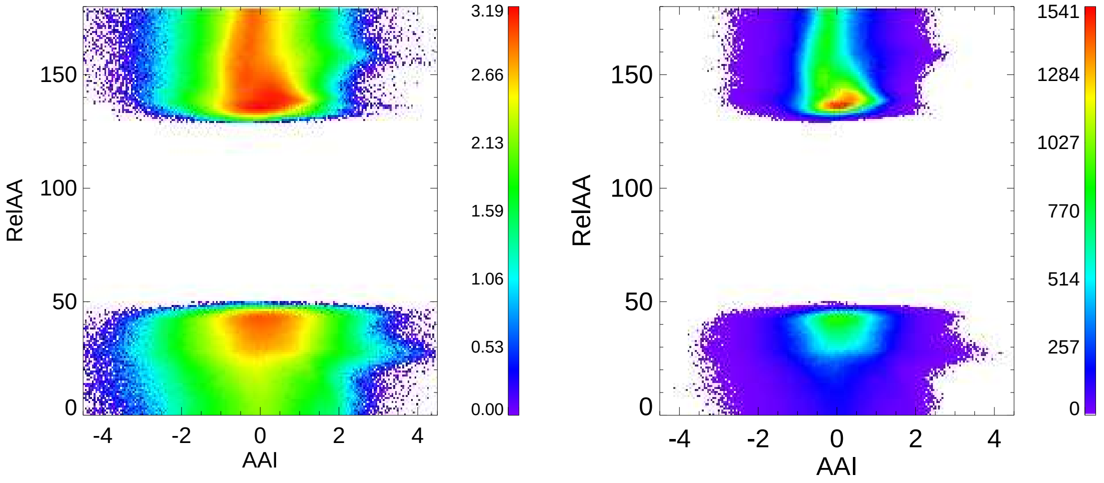

Figure 5.20: GOME-2/Metop-B: Scatter density plot of the distribution of the AAI against the relative azimuth angle (RelAA) on a logarithmic colour scale (left) and a linear colour scale (right).

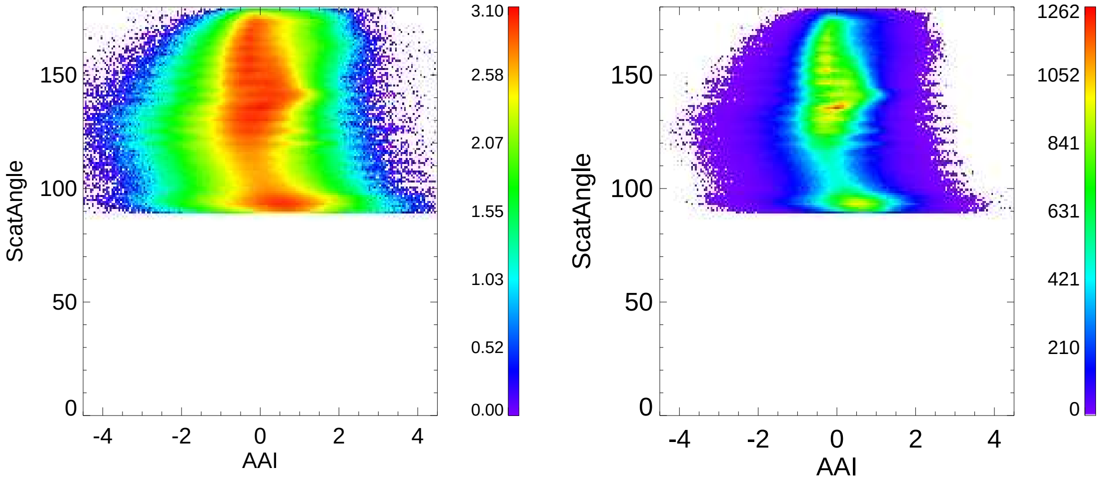

Figure 5.21: GOME-2/Metop-B: Scatter density plot of the distribution of the AAI against the single scattering angle (ScatAngle) on a logarithmic colour scale (left) and a linear colour scale (right).

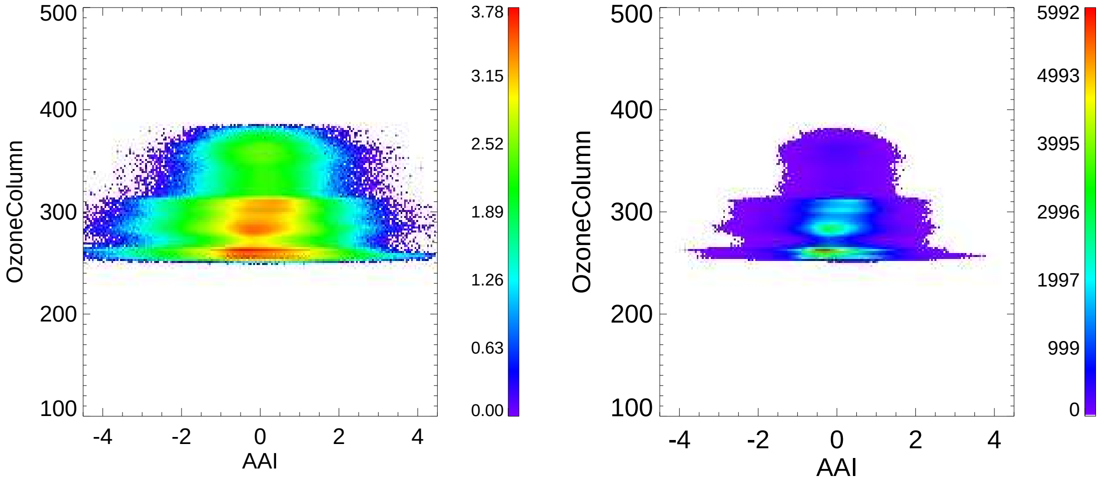

Figure 5.22: GOME-2/Metop-B: Scatter density plot of the distribution of the AAI against the ozone column on a logarithmic colour scale (left) and a linear colour scale (right).

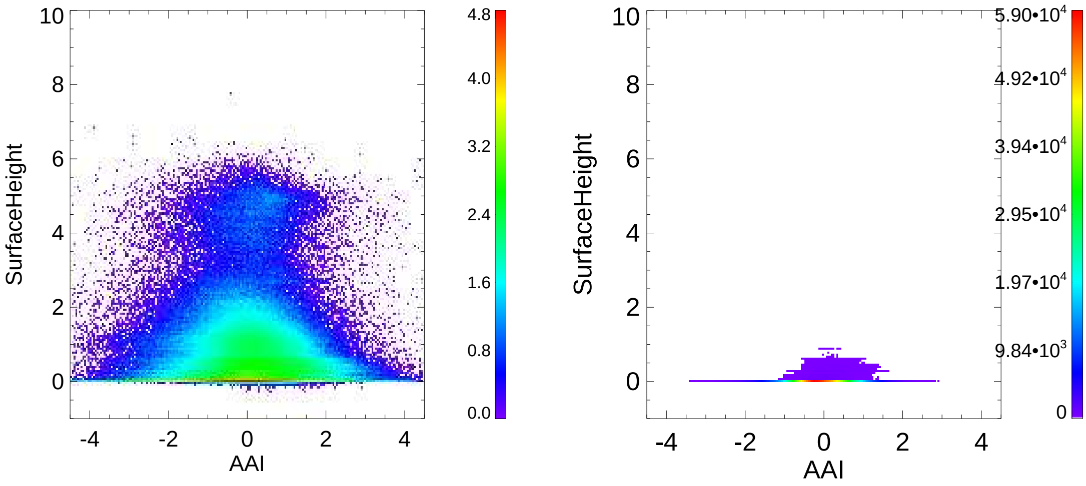

Figure 5.23: GOME-2/Metop-B: Scatter density plot of the distribution of the AAI against the surface height on a logarithmic colour scale (left) and a linear colour scale (right).

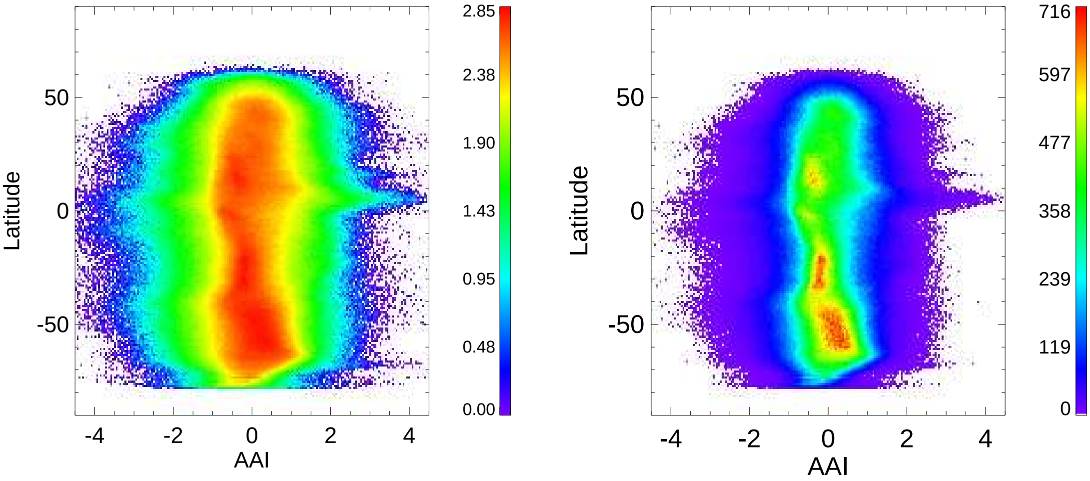

Figure 5.24: GOME-2/Metop-B: Scatter density plot of the distribution of the AAI against the latitude on a logarithmic colour scale (left) and a linear colour scale (right).

Chapter 6

AAI products from the PMD bands

6.1 Short introduction

The previous chapters of this report have all dealt with the verification of the GOME-2 AAI products as derived from the main science channels (MSC). For the MSC AAI products the reflectances are determined from two wavelength regions in spectral channel 2. The size of the MSC measurement footprints amounts to roughly 80×40 km^2. The O3M SAF also produces AAI products derived from polarisation measurement device (PMD) band measurements. The PMD AAI algorithm responsible for this uses reflectances measured by PMD bands 5 and 7, currently configured to wavelengths of 338 and 382 nm. The main advantage of the PMD AAI product is the smaller footprint size of roughly 10×40 km^2.

6.2 Aerosol maps

Figures 6.1 and 6.2 present two images of GOME-2 PMD AAI as measured on 1 June 2013 from the Metop-A and Metop-B platforms, respectively. First of all, the structure of the AAI fields in the two images are very similar. They should be, as there is only a 50 minute gap between the two satellite platforms. The location of the aerosol plumes, in this case the desert dust plumes of Africa, and the desert dust plumes being transported over the Atlantic Ocean, as well as the biomass burning aerosol plumes, are correct. Please note that the more blueish colour of the AAI field measured by GOME-2 from Metop-A is explained entirely by the instrument degradation that was inflicted on Metop-A.

6.3 Statistical analyses

Verification is performed in the way it was done in Chapter 5 for the MSC AAI. Note that the algorithm for the PMD AAI is very similar to that of the MSC AAI after the point at which the reflectances are determined. We therefore only expect significant differences caused by the difference in wavelength pair, and differences caused by differences in radiometric calibration (and instrument degradation).

6.3.1 Metop-A

In Fig. 6.3 we present a statistical verification of the PMD AAI from GOME-2/Metop-A. The plot shows time series of the global mean of the PMD AAI as a function of time. Only a fraction of the 192 PMD scan mirror positions of the forward scan are shown (see colour bar). The jump indicated by the first thick vertical line is explained by the fact that before this date (11 March 2008) the definition of the PMD

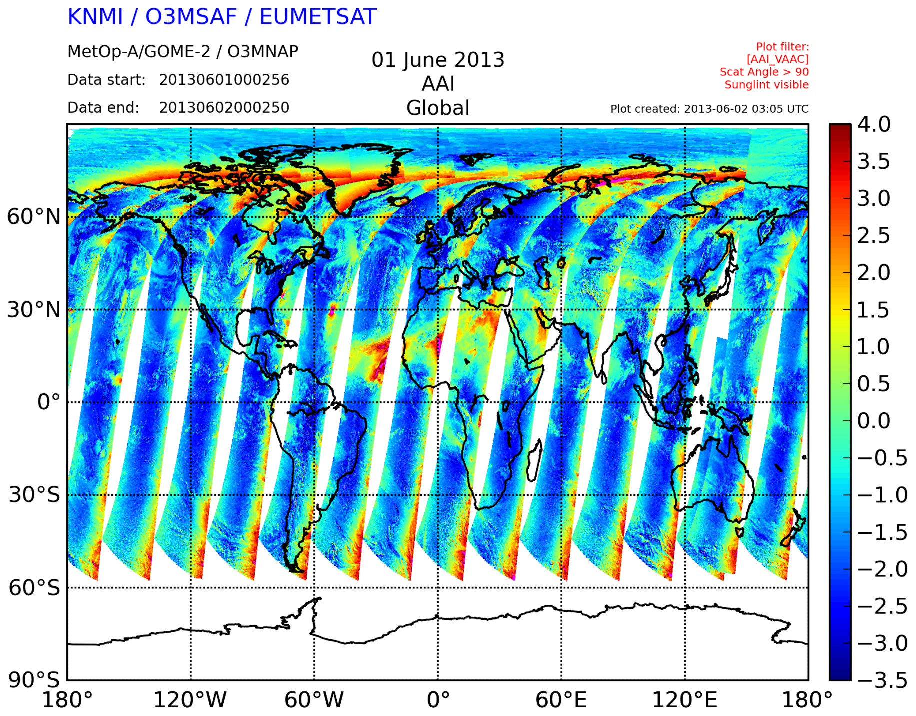

Figure 6.1: Global image of the PMD AAI measured by GOME-2/Metop-A on 1 June 2013. Sunglint filtering was not applied. Desert dust is transported over the Atlantic Ocean.

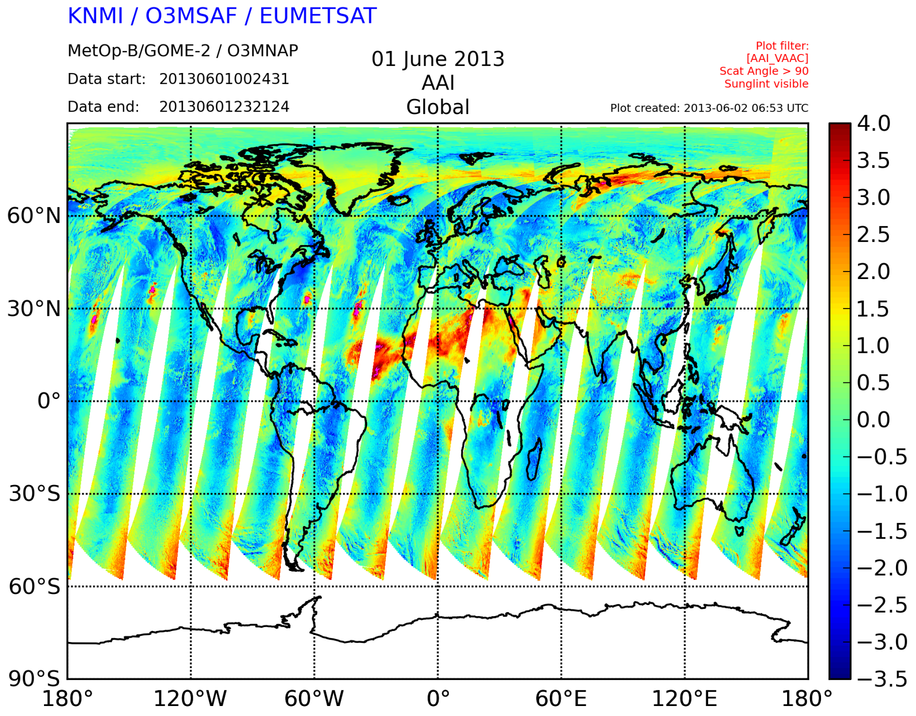

Figure 6.2: Global image of the PMD AAI measured by GOME-2/Metop-B on 1 June 2013. The general structure of the image is similar to the one shown in Fig. 6.1, indicating that the GOME-2 instruments on Metop-A and Metop-B are producing consistent data. Note that GOME-2 on Metop-A produces lower values as a direct result of instrument degradation.

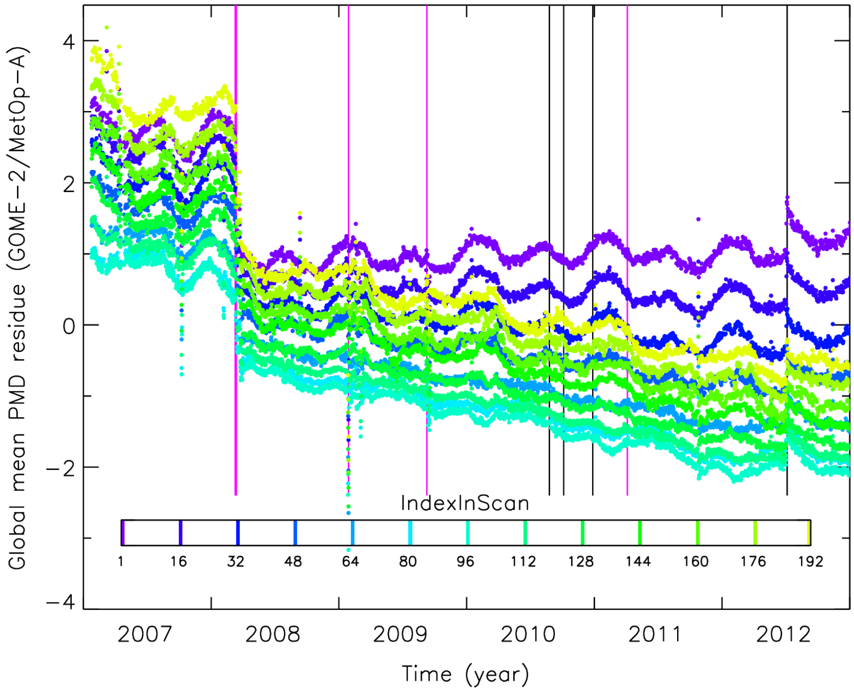

Figure 6.3: Daily global mean PMD residue versus time for a selection of the 192 forward scan mirror positions inside the GOME-2/Metop-A PMD swath.

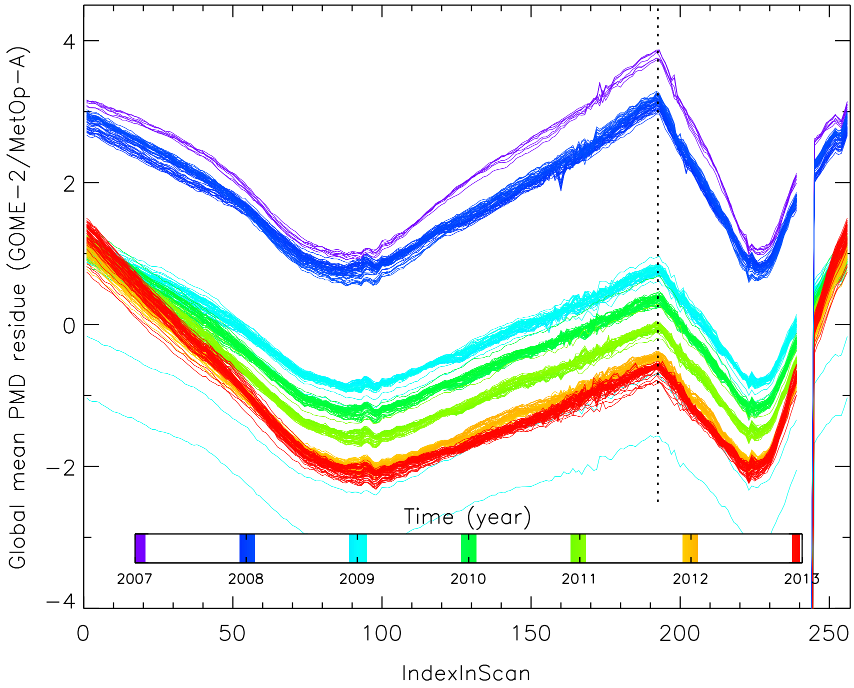

Figure 6.4: Global mean PMD residue measured by GOME-2 on the Metop-A platform as a function of scanner mirror position. Compare with Fig. 5.4. The jump caused by the PMD band definition change, which was introduced on 11 March 2008, is clearly visible.

bands was different. Data from before this date are therefore not consistent with data from after this date. As a result, PMD AAI data from before the PMD band definition change are not made public.

The results from after the jump are very comparable to those of the MSC version. Some small differences are there, but these can be explained by the fact that there are differences in the wavelength definition of the PMD bands. The wavelengths of the PMD bands currently used are 338 (PMD 5) and 382 nm (PMD 7). For the MSC AAI these wavelength were set to 340 and 380 nm, respectively. Also, calibration issues are known to be present in the reflectances retrieved by the PMD bands [*Tilstra et al.*, 2011b]. Nevertheless, the agreement with the MSC time series is satisfactory.

The temporal behaviour of the time series is comparable with that of the MSC AAI time series. The long-term trends, governed mainly by instrument degradation, are also similar. Some differences are there, explained by the fact that the PMD bands and the main science channels degrade in a different manner. The time series of the PMD AAI confirm that a correction for instrument degradation is needed for the PMD AAI products as soon as possible as well.

In Fig. 6.4 we present the same global mean PMD residue, but now as a function of scan mirror position. Backscan measurements are also shown, the scan mirror position therefore runs from 1 to 256. The vertical dotted line indicates the turning point, where the scan mirror changes direction of movement. Note that the retrieval at scan mirror positions 240–244 fails. Pixels 240–243 are known as reset pixels [*Munro and Eisinger*, 2006], and do not produce valid measurements. Pixel 244, next in line after the reset pixels, produces radiances which are not to be trusted. The derived AAI values of pixels 240–244 are, therefore, not be used. Note that these measurements are from backward scan of the instrument.

Comparing Fig. 6.4 with Fig. 5.4 we conclude that there is good agreement with the MSC AAI product. The offset with respect to the MSC AAI from GOME-2/Metop-A is $\sim$0.3 index points if we look at the situation in April 2008, directly after the PMD band definition change, and in the early years of the mission, where the impact of instrument degradation is moderate. This offset of $\sim$0.3 index points is relatively small considering the fact that the AAI is very sensitive to changes/differences in radiometric calibration. For the later years the differences between the AAI of both instruments increase, as a result of the different ways in which instrument degradation affects the main science channels and the PMDs.

6.3.2 Metop-B

The global mean PMD residue as a function of scanner mirror position, presented in Fig. 6.5, clearly shows that the global mean GOME-2/Metop-B PMD residue is in reasonable agreement with the global mean GOME-2/Metop-B MSC residue presented in Fig. 5.6. The upper limit reached at the eastern and western ends of the swath is roughly 1.0 index points, which is the same value found in Fig. 5.6. However, the limit reached around exact nadir is roughly -1.0 index points, which in Fig. 5.6 is about -0.5 for the MSC case. Differences in radiometric calibration are the most likely explanation.

In Fig. 6.5, data from the period between 4 and 12 March 2013 were filtered out, because in this period Metop-B operated in a 960 km wide swath mode.

6.4 Discussion of results

From the verification results that were presented in this Chapter, we conclude that the PMD AAI does not behave any different than its MSC counterpart. This is as expected, because the retrieval algorithms are very comparable. The Metop-A and Metop-B based products show very similar results. For Metop-A, instrument degradation is reducing the quality of the PMD AAI for the later years, just as it is doing that for the MSC AAI from Metop-A. A correction is therefore needed as soon as possible.

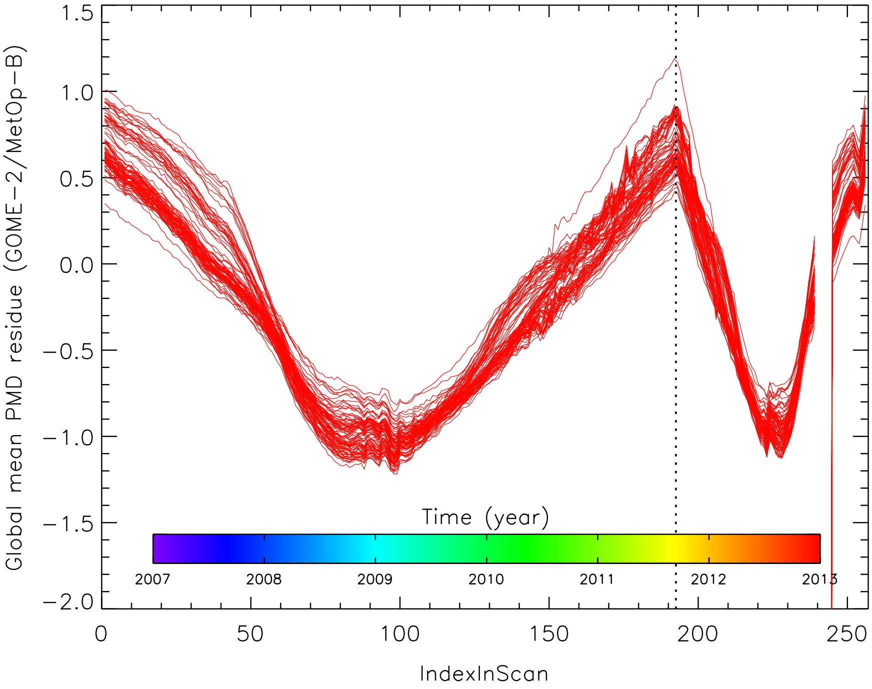

Figure 6.5: Global mean PMD residue measured by GOME-2 on the Metop-B platform versus scanner mirror position. Compare with Figs. 5.6 and 6.4.

Chapter 7

Discussion and conclusions

Because the AAI is calculated from the difference in reflectance at two UV wavelengths, it is not possible to directly relate it to a single aerosol quantity [*de Graaf et al.*, 2005]. The AAI is not a physical quantity but a unitless index. It is therefore hard to do a quantitative verification, or an intercomparison between GOME-2 and other instruments. In the sections below, we will indicate a number of parameters that affect the AAI retrieval, and the quantitative comparison between the GOME-2 AAI and the OMI-TOMS AAI or SCIAMACHY AAI. After that, we will draw conclusions from the results.

7.1 Error sources

7.1.1 Calibration

The AAI strongly depends on the radiometric calibration of the reflectance. An error of 2.3% in one of the two reflectances causes a difference of one entire AAI unit [*de Graaf et al.*, 2005]. Effects of changes in key data, radiometric calibration, or polarisation corrections will show up directly in the retrieved AAI values. This is apparent in the GOME-2 PPF change on 26 June 2008 which caused a shift of about +2 index points in the AAI in the eastern part of the swath.

7.1.2 Wavelength pair

The choice of the wavelength pair affects the retrieval of the residue due to the wavelength dependency of the Rayleigh scattering in the atmosphere. In *de Graaf et al.* [2005] the difference in the AAI values of the wavelength pairs 331/360 nm and 340/380 nm is estimated to be about 25%, with the 331/360 nm AAI being smaller than the 340/380 nm AAI. Also see Chapter 4 of this document.

7.1.3 Viewing geometry

The paper by *de Graaf et al.* [2005] has shown that the residue (AAI) value is affected by the viewing geometry. For instance, for a relative azimuth angle of 0^0 the residue varies with increasing total scattering angle across the full range of 0.75 to 4.0 index points for a test case (aerosol between $3-4$ km, $\tau = 1.0$, $\omega_0 = 0.9$ and a surface albedo of 0.05). For a representative GOME-2 situation (SZA of 40^0 and 0^0–50^0 viewing zenith angle range) the retrieved AAI varies between 0.75 and 1.0 index points for the same aerosol case. For relative azimuth angles of 90^0 and 180^0 the effect of the geometry is considerably smaller (the full ranges are 0.8–1.5 and 0.9–1.3, respectively).

7.1.4 Ozone column

The residue is sensitive to ozone absorption, especially at the smaller wavelength of the wavelength pair. The reduction of the TOA reflectance by ozone absorption goes approximately with $exp(-\tau_{O_3}M)$ where $M = 1/\mu_0 + 1/\mu$. In the AAI algorithm the exponent is approximated by $1 - \tau_{O_3}$ [*de Graaf et al.*, 2005], where the total ozone column comes from an ozone climatology (interpolated to month and latitude). It would be better to use the actual ozone column in the algorithm, especially when the real column is more than 100 DU different from the approximated value used in the calculation. In this extreme case, the residue can be a whole index point off. (L.G. Tilstra, personal communication, 2008).

7.1.5 Summary of error sources

In Table 7.1 we summarise the error sources and indicate the effect on the AAI expressed in points (pt).

Error Source	Error Range	Remarks
Radiometric Calibration	2 pt	PPF 3.9.0 to 4.0.0, eastern side
Wavelength Pair	25 %	
Solar Zenith Angle	$0.1 - 0.2$ pt	difference between east and west
Viewing Zenith Angle	$0.1 - 1.0$ pt	crosstrack variation
Ozone Column	$<= 1.0$ pt	for differences up to 100 DU

Table 7.1: Error sources in the GOME-2 AAI.

7.2 Accuracy of intercomparisons

7.2.1 GOME-2 versus OMI-TOMS

From the list of error sources above, some effects have to be taken into account in the intercomparison of GOME-2 and OMI-TOMS AAI values. Assuming that the calibration of both instruments is perfect and that the ozone column is known (or the climatological column is close enough to the real column), we mainly have to consider:

- The difference in overpass time: at 13:45 LT, OMI sees the atmosphere when the convection has been more developed than GOME-2 (at 09:30 LT). Aerosol can be transported to higher levels, leading to an increased residue value for OMI.
- The viewing geometry of the two instruments is different. OMI also has a smaller SZA than GOME-2, due to its overpass time closer to local noon. This means a difference of 0.1–0.2 in AAI. The viewing angles of OMI are larger at the extremes of the swaths (also leading to a difference of approximately 0.1–0.2 points in AAI). Finally, the relative azimuth is very different, leading to differences of about 0.1–1.0 index points.
- The wavelength pair used in the retrieval of the two instruments is different: 340/380 nm for GOME-2 and 331/360 nm for OMI-TOMS. As mentioned above, this can lead to a 25% difference in the AAI. As a consequence, a GOME-2 AAI of 2 index points may actually correspond to a OMI-TOMS AAI of 1.5 index points (also see Chapter 4).
- The spatial resolution of the two instruments is different. The pixel size of GOME-2 is about 9 times larger than the OMI pixel size at nadir. Thus the local AAI peaks in GOME-2 will be smaller due to averaging effects.

Combining the above positive and negative AAI differences between GOME-2 and OMI-TOMS, we can explain differences of the order 0.1–1.0 points.

7.2.2 Other findings

From a visual intercomparison of many GOME-2 AAI and OMI-TOMS AAI, not all shown in this report, but similar to the ones presented in Chapter 2, we can draw the following findings:

- The location of the GOME-2 AAI generally corresponds to that of the OMI-TOMS AAI.
- The main aerosol events are well detected by GOME-2, although the peak GOME-2 values are lower than those of OMI-TOMS.
- In the region north of 70°N, there is a general tendency to overestimate the GOME-2 AAI values. This is possibly due to high solar zenith angles.
- There is a 'C-shape' present in the GOME-2 AAI data, related to the treatment of the polarisation parameters.
- South of the lower end of the C-shape, in the SH mid-latitudes, there is still an east-west bias present in the AAI results.

7.2.3 GOME-2 versus SCIAMACHY

SCIAMACHY is the ideal instrument to compare with, for a number of reasons:

- SCIAMACHY is, like GOME-2, in a descending orbit with an almost identical orbital period.
- The equator passing times of SCIAMACHY (10:00 LT) and GOME-2 (09:30 LT) are only 30 minutes apart.
- The residue wavelength pair is completely identical.
- The viewing geometry for collocated orbits is identical. The solar geometry is different by only 30 minutes in time, resulting in a maximum difference between the SCIAMACHY and GOME-2 solar zenith angles of 7° only, leading to residue differences of no more than 0.2 index points.

The errors caused by the overpass time difference of 30 minutes is small compared to the error caused by the fact that the SCIAMACHY and GOME-2 footprints do not perfectly overlap. We estimate, from an analysis of the statistics of Fig. 3.2, that this can explain errors up to 0.5 index points for individual measurements. However, many measurements are used to analyse each day of data.

7.3 Common feature in OMI and GOME-2 AAI

As mentioned in the last point in Section 7.2.2, there exists a common feature in the OMI and GOME-2 AAI at high latitudes in the SH. The feature is for GOME-2 present at the east side of the swath, and for OMI at the west side of the swath.

This phenomenon is at the moment still under investigation. However, we can already report a few first results on this issue. First of all, the exact location inside the GOME-2 orbit where the phenomenon occurs seems to be closely related to the scattering geometry of the problem. This would at least explains why the phenomenon is found at the east side of the swath for GOME-2, and at the west side of the swath of the OMI orbit. (GOME-2 is in a descending morning orbit, overpass time at the equator of 09:30 LT, and OMI is in an ascending afternoon orbit, with an overpass time at the equator of 13:45 LT).

Secondly, the phenomenon is present in each orbit, at the same position in the orbit, irrespective of the underlying surface type. It is there for clouded scenes, and also for unclouded scenes. This would indicate that the phenomenon is not governed by the scene (reflectances) itself.

A third observation is that the position and strength of the phenomenon is moving throughout the year, following a seasonal cycle. This would indicate a dependence on solar zenith angle (SZA), in other words, a dependence on the scattering geometry of the problem.

From direct comparison with SCIAMACHY (the SCIAMACHY–GOME-2 comparison in the validation report) we could at least confirm that the GOME-2 viewing and solar geometry (in particular the azimuth angles describing the problem), as used in the code for the AAI retrieval, are OK.

The phenomenon seems to be a property of the AAI. We are at the moment investigating whether this is indeed the case.

7.4 Conclusions

From the results of the SCIAMACHY–GOME-2 comparison we conclude that the GOME-2 MSC AAI is of good quality. This we conclude from the good (one-to-one) correlation between GOME-2 and SCIAMACHY residues. The offset between GOME-2 and SCIAMACHY residues is found to be close to zero, but shows a slightly negative trend over the time period studied. This we have to attribute to the effects of instrument degradation. Because of the way in which the intercomparison was conducted, the results only apply to that part of the GOME-2 swath that overlaps with the SCIAMACHY swath. This is basically the part of the GOME-2 swath that coincides with the GOME-1 swath width. For completeness, we should also mention that the result only applies to the forward scan measurements of GOME-2, because the intercomparison was performed using forward scan pixels only.

In the Product Requirements Document (PRD) [*Hovila et al.*, 2009], the accuracy requirements for the AAI product are given as follows. The "threshold level" is set to 1.0 index points, the "target level" is set to 0.5 index points, and the "optimal level" is set to 0.2 index points. As the bias-corrected uncertainty in the GOME-2 MSC AAI was found to be ∼0.5 index point (determined from the results of the intercomparison with the SCIAMACHY instrument), we conclude that the (bias-corrected) value of 0.5 index points relates well to the target uncertainty of 0.5 index points mentioned in the PRD.

The visual comparison with OMI-TOMS data was useful as it confirmed that the global aerosol distribution is well described by global maps of the GOME-2 AAI. However, the comparison pointed to a positive offset, while the SCIAMACHY–GOME-2 comparison pointed to a near-zero offset. The explanation for this discrepancy is described and can be found in Section 7.2.1.

The statistical analyses allow more quantitative studies into the dependencies of the AAI on relevant parameters as scan mirror position, the precise scattering geometry, latitude et cetera. The global mean MSC residue in particular revealed a similar seasonal variation for GOME-2 (on Metop-A) as was found earlier for GOME-1. However, a modest offset of ∼0.4 index points w.r.t. the GOME-1 global mean value was found. When the calculation was repeated taking only those measurements that are located in the inner (GOME-1) part of the GOME-2 swath, the offset was reduced to ∼0.2 index points. Note that this is roughly equal to the near-zero offset we found from the SCIAMACHY–GOME-2 comparison.

For GOME-2 on Metop-B we found the MSC AAI to agree nicely with the MSC AAI from the Metop-A platform. Only a small offset of ∼0.3 index points seems to be present. This value is representative only for data directly after launch of the instruments, where instrument is not an issue yet.

The PMD AAI from Metop-A and Metop-B show similar behaviour as the MSC AAI products. The statistical analyses show that the PMD AAI from Metop-A is very close to the MSC AAI from Metop-A. A small offset of 0.3 index points is found. The PMD AAI from Metop-B compares reasonably with the MSC AAI from Metop-B. An explanation for the differences is the (known) different radiometric calibration between MSC reflectances and PMD reflectances.

In conclusion, the GOME-2 AAI is in a good shape, but instrument degradation has a strong impact on the quality of the AAI product from Metop-A. This is expected to become an issue for the AAI from Metop-B in the near future. A proper correction for instrument degradation is therefore needed.

Note that the verification presented in this report was applied to data to which a correction for instrument degradation was not applied.

Bibliography

Bovensmann, H., J. P. Burrows, M. Buchwitz, J. Frerick, S. Noël, V. V. Rozanov, K. V. Chance, and A. P. H. Goede (1999), SCIAMACHY: Mission objectives and measurement modes, *J. Atmos. Sci.*, *56*, 127–150.

de Graaf, M., P. Stammes, O. Torres, and R. B. A. Koelemeijer (2005), Absorbing Aerosol Index: Sensitivity analysis, application to GOME and comparison with TOMS, *J. Geophys. Res.*, *110*, D01201, doi:10.1029/2004JD005178.

de Graaf, M., O. N. E. Tuinder, and L. G. Tilstra (2010), O3MSAF Algorithm Theoretical Basis Document for ARS, *O3MSAF/KNMI/ATBD/002, Issue 1.0*, KNMI.

Hovila, J., S. Kiemle, O. Tuinder, H. Joench-Soerensen, and F. Karcher (2009), O3M SAF Product Requirements Document, *SAF/O3M/FMI/RQ/PRD/001, Issue 1.0*, O3M SAF.

Munro, R., and M. Eisinger (2006), GOME-2 Level 1 Product Generation Specification, *PGS v6.1*, EUMETSAT.

Tilstra, L. G., M. de Graaf, I. Aben, and P. Stammes (2007), Analysis of 5 years SCIAMACHY Absorbing Aerosol Index data, in *Proceedings of the 2007 Envisat Symposium, ESA Special Publication SP-636*, European Space Agency, ESA/ESTEC, Noordwijk, The Netherlands.

Tilstra, L. G., O. N. E. Tuinder, and P. Stammes (2010), GOME-2 Absorbing Aerosol Index: Statistical analysis, comparison to GOME-1 and impact of instrument degradation, in *Proceedings of the 2010 EUMETSAT Meteorological Satellite Conference*, EUMETSAT P.57.

Tilstra, L. G., M. de Graaf, O. N. E. Tuinder, R. J. van der A, and P. Stammes (2011a), Studying trends in aerosol presence using the Absorbing Aerosol Index derived from GOME-1, SCIAMACHY, and GOME-2, in *Proceedings of the 2011 EUMETSAT Meteorological Satellite Conference*, EUMETSAT P.59.

Tilstra, L. G., O. N. E. Tuinder, and P. Stammes (2011b), GOME-2 PMD band reflectances – verification report, *KNMI Report KNMI-RP-2011-01, Issue 2.0*, KNMI.

Tilstra, L. G., M. de Graaf, I. Aben, and P. Stammes (2012), In-flight degradation correction of SCIAMACHY UV reflectances and Absorbing Aerosol Index, *J. Geophys. Res.*, *117*, D06209, doi: 10.1029/2011JD016957.